



ASME Accepted Manuscript Repository

Institutional Repository Cover Sheet

First

Last

ASME Paper Title: Assessment of the Robustness of a Fixtureless Inspection Method for Nonrigid Parts Based on a

Verification and Validation Approach

Authors: Sasan Sattarpanah Karganroudi, Jean-Christophe Cuillière, Vincent François, Souheil-Antoine Tahan

ASME Journal Title: Journal of Verification, Validation and Uncertainty Quantification

Volume/Issue

volume: 2, issue : 4 _____

Date of Publication (VOR* Online)

February 13 2018 _____

ASME Digital Collection URL: <https://asmedigitalcollection.asme.org/>

DOI: <https://doi.org/10.1115/1.4038917>

*VOR (version of record)

Assessment of the robustness of a fixtureless inspection method for nonrigid parts based on a verification and validation approach

Sasan Sattarpanah Karganroudi¹, Jean-Christophe Cuillière¹, Vincent François¹, Souheil-Antoine Tahan²
¹Équipe de Recherche en Intégration Cao-CALcul (ÉRICCA), Université du Québec à Trois-Rivières, Trois-Rivières, Québec, Canada
²Laboratoire d'ingénierie des produits, procédés et systèmes (LIPPS), École de Technologie Supérieure, Montréal, Québec, Canada

Abstract

The increasing practical use of Computer-Aided Inspection (CAI) methods requires assessment of their robustness in different contexts. This can be done by quantitatively comparing estimated CAI results with actual measurements. The objective is comparing the magnitude and dimensions of defects as estimated by CAI with those of the nominal defects. This assessment is referred to as setting up a validation metric. In this work, a new validation metric is proposed in the case of a fixtureless inspection method for non-rigid parts. It is based on using a nonparametric statistical hypothesis test, namely the Kolmogorov–Smirnov (K-S) test. This metric is applied to an automatic fixtureless CAI method for non-rigid parts developed by our team. This fixtureless CAI method is based on calculating and filtering sample points that are used in a finite element non-rigid registration (FENR). Robustness of our CAI method is validated for the assessment of maximum amplitude, area and distance distribution of defects. Typical parts from the aerospace industry are used for this validation and various levels of synthetic measurement noise are added to the scanned point cloud of these parts to assess the effect of noise on inspection results.

Keywords

Fixtureless inspection, verification and validation, V&V, non-rigid parts, GNIF, principal curvatures, von Mises stress, hypothesis testing, metrology, inspection.

1. Introduction

High-quality standards that are applied in many industrial sectors, among which aerospace and automotive industries, require setting up robust, rapid and accurate quality control processes. Geometric Dimensioning and Tolerancing (GD&T) and automated inspection are two key aspects of this issue. Automating inspection can be performed using non-contact scanning devices but automated inspection still faces many challenges. Automating the inspection of non-rigid parts is part of these challenges. It remains a serious problem since these parts may deform during the inspection. These parts may deform under their own weight and also from residual stress that is eventually induced by manufacturing and handling processes. Compliance is a measure of flexibility for non-rigid parts and it is defined as the ratio between the deformation of the part induced by a force and the applied force [1]. Referring to this definition, a manufactured part is considered as non-rigid if the deformation induced by a reasonable force (around 40 N) is 10% higher than specified tolerances. Based on standards in metrology such as ASME Y14.5 and ISO-GPS, the inspection of parts is performed in a free-state, except for non-rigid parts, as it is mentioned in ISO-10579 and ASME Y14.5 (2009). Free-state refers to a situation in which a manufactured part is not submitted to any other load than its own weight. As it is illustrated in Figure 1-a, a non-rigid aerospace panel in a free-state deforms due to its compliance under its own weight. Based on conventional dimensioning and inspection methods for non-rigid parts, very sophisticated and expensive inspection fixtures need to be designed and used to compensate for flexible deformation of these parts during inspection. Setting up and operating these inspection fixtures is time-consuming and expensive. Figure 1-b illustrates an example of such an inspection fixture for the part shown in a free-state in Figure 1-a.

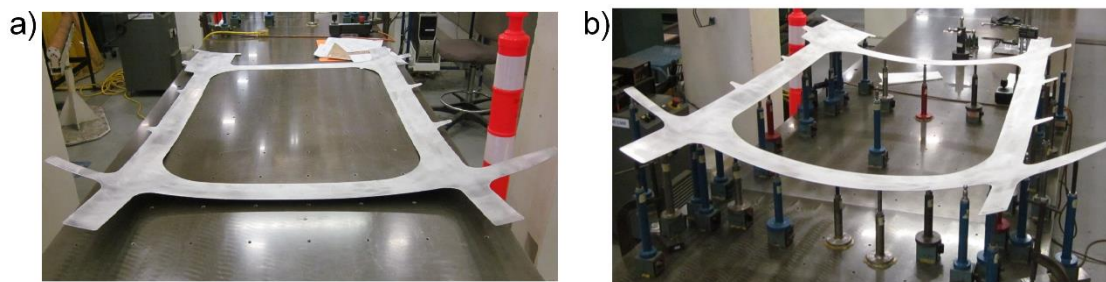


Figure 1: A regular aerospace panel, a) in free-state, b) constrained by fixing jigs on the inspection fixture [2]

Recent improvements in data acquisition devices, such as three-dimensional (3D) scanners, and in computational calculations, allow an ongoing progress towards *Computer-Aided Inspection* (CAI) methods. These methods facilitate inspection by using a comparison between the scan model of a manufactured part and its *Computer-Aided Design* (CAD) model. 3D optic and laser scanners allow obtaining triangulation of the surfaces of non-rigid manufactured parts without contact, e.g. without eventual deformation caused by contact with a probe. The raw

output provided by these scanners is a 3D point cloud, from which a triangulated mesh can easily be obtained. Beholden to progress about CAD and CAI methods, fixtureless non-rigid inspection methods [3-12] are developed. These methods consist in virtually compensating for the compliance of non-rigid parts. The first step of all these fixtureless CAI methods for non-rigid parts, referred to as rigid registration, is searching for a rigid transformation matrix between CAD and scanned data. Then the effective core of these methods, referred to as non-rigid registration, consists in trying to find the best correspondence between CAD and scanned data, either by deforming scanned geometry to CAD geometry or by deforming CAD geometry to scanned geometry. The core idea behind these methods is trying to distinguish between flexible deformation of scan model that is inherent to free-state and geometrical deviations associated with defects on the scan model. These non-rigid registration methods thus virtually compensate for the flexible deformation of non-rigid parts in a free-state and allow the estimation of geometrical deviation on the manufactured parts with respect to their CAD model.

In order to apply non-rigid registration methods based on deforming the scan model towards the CAD model, as presented in [3-5], a time-consuming process of generating a FE mesh from the acquired point cloud (scan model in free-state) is required. Then, the scan mesh is deformed by applying a set of constraints in a finite element analysis (FEA). Using feature extraction techniques [13], the displacement boundary conditions (BCs) in *virtual fixation concept* [3] are imposed on fixation features of scan meshes to displace them towards the corresponding features on the CAD model. The developed approach in [4] aims at determining specific displacement BCs that minimize the location and orientation of fixation features between the predicted post-assembly shape (deformed scan model) and CAD model. Inspired by an industrial inspection method in [5], the functional shape of a scan model is retrieved by virtually restraining this deformed scan model under a combination of forces located on datum targets. These constraints are then used to perform a *virtual inspection* on the deformed scan model in its assembly-state. However, generating FE meshes for each measured part and locating appropriate BCs for each scan model hinder automating the inspection process of these CAI methods. Therefore, non-rigid inspection methods based on applying FEA on CAD models instead of scan models have been introduced in [6-12]. Indeed, these non-rigid inspection methods generally use meshes with better quality since these meshes are generated from CAD models. Unlike *virtual fixation concept* [3], displacement BCs used in [6] are imposed on the fixation features of the CAD model. In order to enable a CAI for partially scan models, the location of missing fixation features is approximated in [7] using an interpolating technique. The *iterative displacement inspection* (IDI) algorithm [8, 9] is also a non-rigid CAI method in which smooth and iterative displacement vectors are applied to deform CAD model towards the shape of scan model. The displacement vectors used in IDI are determined through a specific identification algorithm, which allows distinguishing between defects and flexible deformation. However, this identification algorithm in IDI is limited to localized defects, which makes it less general than other approaches. *Generalized numerical inspection fixture* (GNIF) method [10] claims ability to detect both small (local) and big (global) defects. This method generates sets of corresponding sample points on CAD and scan models, which are used as displacement BCs to deform the CAD model towards the scan model through FEA. Applying corresponding sample points on assembly features, along with bounding edges [10] and/or specified pre-selected sample points on the CAD model [11] are obstacles to fully automating the inspection process. In this context, our team developed an automatic fixtureless inspection approach [12] that uses GNIF to generate a prior set of corresponding sample points. Then, sample points that are close to defects are filtered out, based on curvature and von Mises criteria, which leads to an accurate and automatic inspection method for non-rigid parts.

All these fixtureless CAI methods for non-rigid parts are based on using scanned data, which is acquired from scanning devices. It is commonly known that these data acquisition devices introduce measuring errors that are either due to their technical limits or to effects such as light fraction, reflectivity of the scanned surfaces or inaccessible features. Noisy scan data used in fixtureless CAI methods is likely to affect performance of these methods. Therefore, robustness of fixtureless CAI methods for non-rigid parts with respect to noisy scanned data should be assessed. One alternative in doing that is using *Verification and Validation* (V&V) recommendations. Indeed, applying V&V recommendations to computational simulation models allows assessing accuracy and reliability of these models [14]. Verification relates to assessing the accuracy of a solution while validation relates to assessing the consistency of computational simulation results if compared with the actual results. Due to various sources of uncertainty in computer codes and simulations, all computational models should be thoroughly verified and validated.

This paper presents a novel validation metric that is intended to validate the robustness of CAI methods in general. In this paper, it is applied to a fixtureless CAI method for non-rigid parts developed by our team [12] but it can easily be extended to other CAI methods. The paper is organized as follows. Section 2 presents our approach to automatic fixtureless CAI for non-rigid parts. It is followed, in section 3, by an introduction of *ASME Verification and Validation* (V&V) recommendations along with a presentation about how these methods are applied for assessing the robustness of our fixtureless CAI approach for non-rigid parts. Results obtained using our CAI method, along with an assessment of its performance and robustness based on V&V recommendations, are then presented in section 4 and 5. For this, two typical non-rigid parts used in the aerospace industry are considered along

with various distributions of noise in scan data. The paper ends with a conclusion and ideas for future work in section 6.

2. Background on the approach to fixtureless CAI for non-rigid parts

As mentioned in Section 1, we have proposed, in a previous paper [12], a new automatic fixtureless CAI method for non-rigid manufactured parts using scan data in a free-state condition without any conformation or constrain operations. This method is based on *FEA Non-Rigid Registration* (FENR) and on two filters applied on corresponding sample points between scan and CAD models. Basically, these filters allow making a difference between flexible deformation in a free-state and defects. The method is illustrated on a typical non-rigid aluminum panel, which is used in the aerospace industry. The CAD model of this panel is shown in Figure 2-a, and the associated simulated scan model for inspection in a free-state is depicted in Figure 2-b. This scan model includes three bump defects, for which the nominal size and shape are known in order to assess the accuracy and robustness of inspection results. Using simulated scan models instead of real measured scan data allows analyzing results obtained with the CAI method proposed in this paper with respect to the fact that the shape of all defects is accurately known. Indeed, the magnitude of measuring errors (due to inaccuracy of scanners) is usually higher than numerical uncertainties of CAI methods. Thus, in order to better focus on studying numerical errors associated with the CAI approach proposed, synthetic defects, for which amplitude shape and size are a priori known, are used in this study.

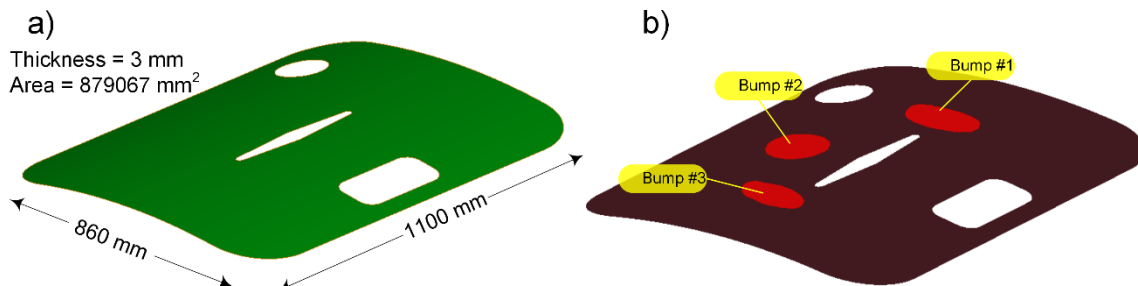


Figure 2: a) 3D view of the CAD model of a non-rigid aluminum panel b) the scan model featuring three bump defects.

A pre-registration, based on the ICP algorithm [15], best fits CAD and scan models through a preliminary rigid registration. Then, the *generalized numerical inspection fixture* (GNIF) [10] method is applied to generate an initial set of evenly distributed corresponding sample points between CAD and scan data in a free-state. Indeed as shown in Figure 3, based on an isometric deformation assumption, on *generalized multi-dimensional scaling* (GMDS) [16] and on computing geodesic distances with the *fast marching method* [17], GNIF generates a list of corresponding sample points on each model (CAD and scan). Since mesh quality of the CAD model is generally better than that of the scan model, *FEA Non-Rigid Registration* (FENR) is applied on CAD mesh. For this, corresponding sample points are inserted as nodes in CAD mesh using a classical Delaunay point insertion method [18]. Displacement boundary conditions are then applied on these nodes, which deforms CAD model towards scan model via FENR. Since these corresponding sample points are evenly distributed over both CAD and scan models, some of these points can be located, close to, or even on defects. If this occurs, it eventually results in an inaccurate estimation of the size of these defects since FENR tends to bring these nodes to the shape of defects. Thus, sample points that are close to defects must be filtered out. As explained in detail in [12], these sample points are successively filtered out based on two criteria: principal curvatures and von Mises stress. The process starts with applying a first FENR based on using all GNIF sample points. By doing that, CAD model is deformed to take on the shape of scan model, including in locations on and around defects. Then, analyzing the difference in principal curvatures between the initial CAD model and the deformed CAD model (after the first FENR) allows a first rough estimate of defects location. A first set of corresponding sample points that are close enough to these estimated defects is removed on both models and a second FENR is applied. The second filtration of sample points is applied, based on analyzing von Mises results obtained from this second FENR, which allows a better estimation of defects since some more sample points are filtered out. A third and last FENR is performed from sample points remaining. Initial GNIF corresponding sample points on the CAD model, as shown in Figure 4, are illustrated as red spots (●) while filtered sample points are illustrated as blue spots (●).

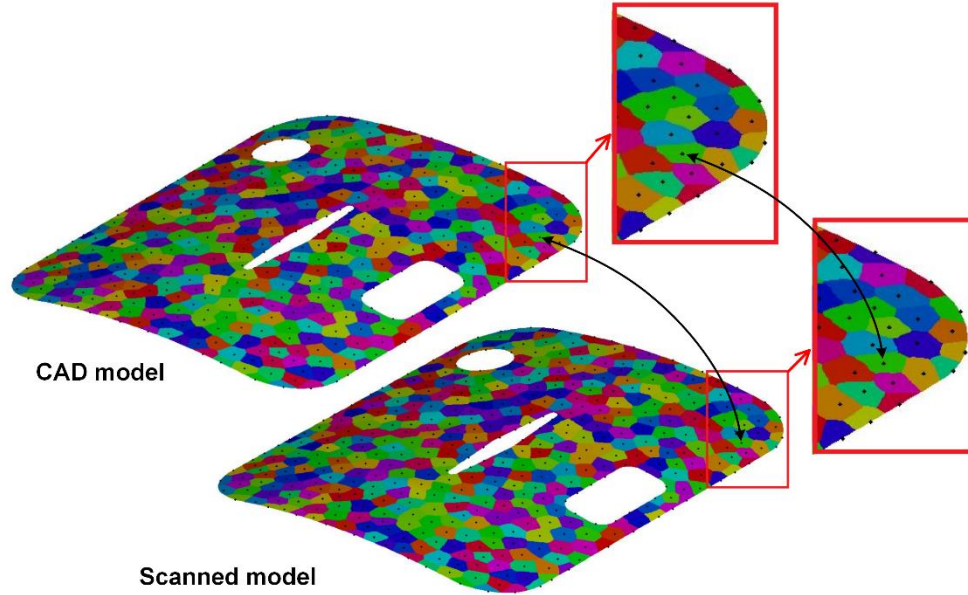


Figure 3: GNIF corresponding sample points (in black) are located in the center of colorful zones on the CAD and scan models.

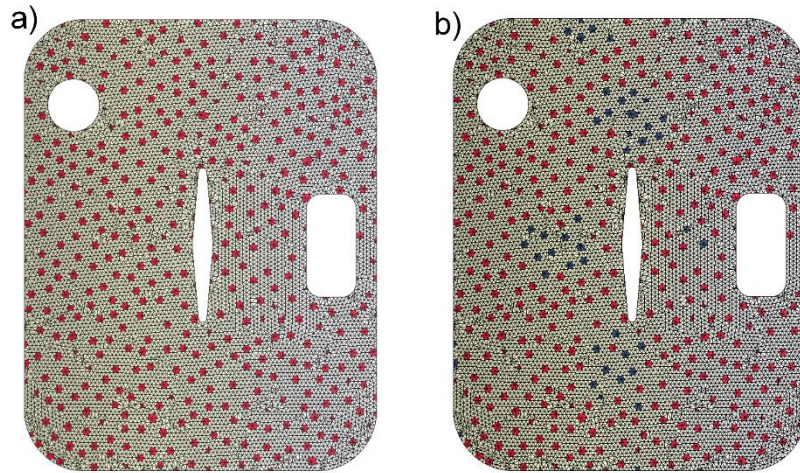


Figure 4: a) all GNIF sample points inserted into the CAD mesh based on classical Delaunay method (red spots) b) automatic sample point filtration based on curvature and von Mises stress criteria and criteria (blue spots).

Once this last FENR applied (in red in Figure 4-b) the CAD model is deformed to the scan model in a free-state condition and color map of Euclidean distance distribution between the two models can be plotted. This graphical representation (shown in Figure 6-a) allows assessing the magnitude of defects with respect to the specified tolerance. According to ASME Y14.5 and ISO-GPS profile tolerance definition, defects are defined as zones for which the actual manufactured part deviates from the specified geometry, with respect to a tolerance value as specified on detailed engineering drawings. For all validation cases presented in this paper, ± 0.4 mm is considered as specified profile tolerance. 0.8 mm is indeed a representative geometric profile tolerance value for the type of thin-walled aerospace parts used in this paper. For a given part, N_{defect} refers to the number of defects identified on the scan model. As shown in Figure 5, at the location of a given defect, the maximum deviation between the deformed CAD (after FENR) and scan model occurs at tip or valley of the defect i (wherein $i = 1, \dots, N_{defect}$). This deviation is referred to as the maximum amplitude of the defect i (D_i^{max}). At the location of a given defect we also assess the area of each defect. As illustrated in Figure 5, this area (A_i) is defined as the region of the deformed CAD (after FENR) that is at a distance, from the scan model, that exceeds the tolerance value. In Section 3.2, the analysis of defects will be pushed one more step forward by assessing the distance distribution of defects.

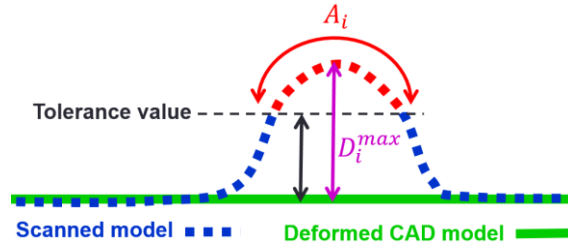


Figure 5: Definition of maximum amplitude D_i^{max} and area of a defect A_i .

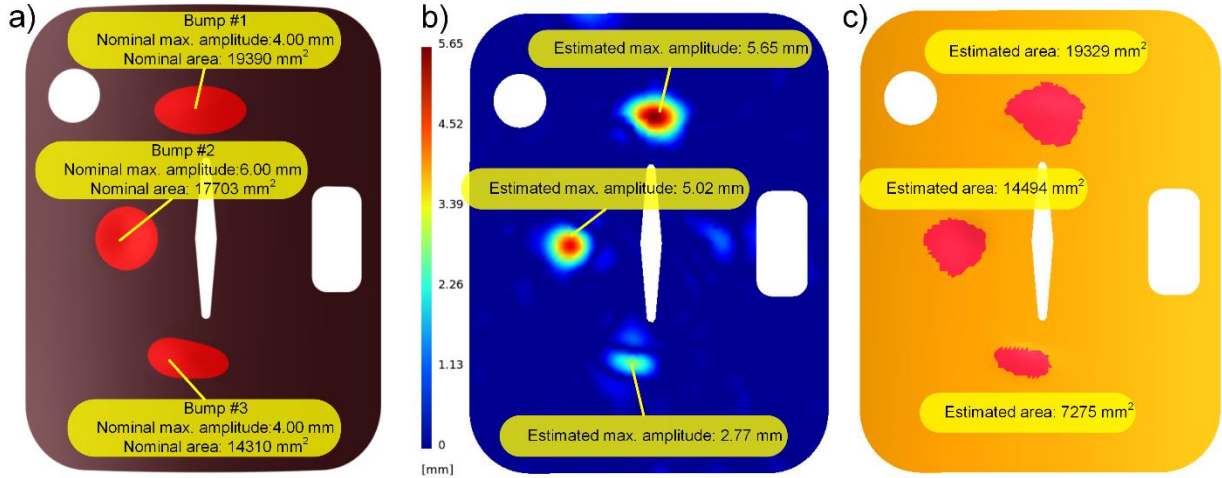


Figure 6: a) the scanned part with the nominal dimensions of defects b) estimated and nominal maximum amplitude (D_i^{max}) of defects [mm] c) estimated and nominal area (A_i shown as red zones) of defects [mm²].

The flowchart of our automatic fixtureless CAI method for non-rigid parts is illustrated in Figure 7. It shows that our CAI inspection method uses scan data, the CAD model, and a specified profile tolerance as input. Then using the GNIF method, sets of corresponding sample points are generated on CAD and scan models. Sample points that are located around or on defects are filtered out and the CAD model is deformed towards the scan model, to compensate for free-state deformation of the scanned part. The output of this inspection process consists of a global distance distribution, as a color map, the number of identified defects (N_{defect}) along with maximum amplitude (D_i^{max}) and its area (A_i) of each defect i .

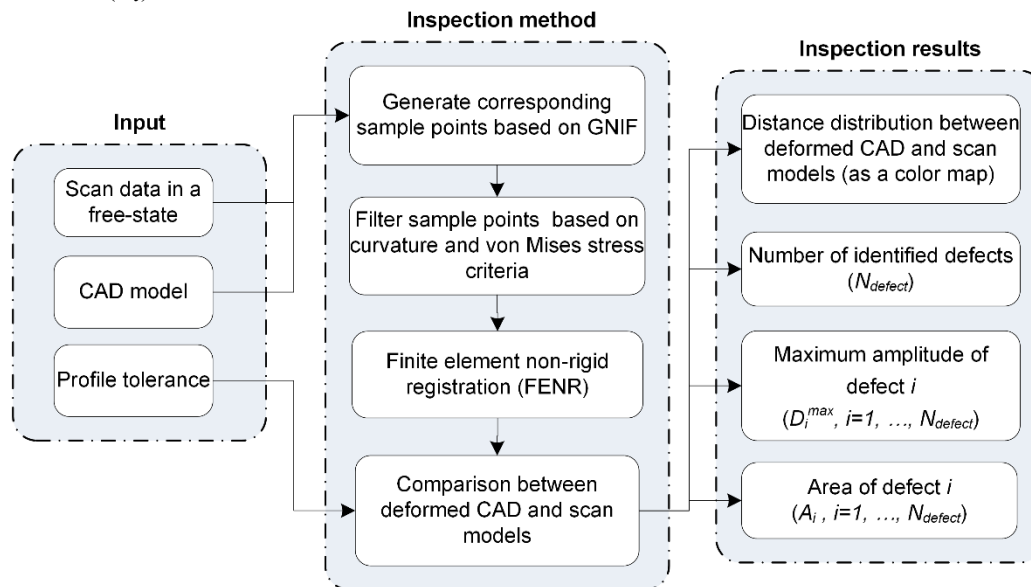


Figure 7: Flowchart of our automatic fixtureless CAI method.

Indeed, the quality of all measuring systems must be assessed. This ensures that the generated measuring data satisfy requirements of the measured process. In this context, the measuring system is referred to as the collection of instruments or gages, standards, operations, methods, fixtures, software, personnel, environment and etc. A general

guideline for assessing measurement system acceptability states that a measurement system is considered as unacceptable if measurement variation exceeds 30% [19]. To this end, results obtained in estimating D_i^{max} (Figure 6-b) and A_i (Figure 6-c) of the three defects, in the part introduced in Figure 6-a, show that estimated inspection results are promising. Indeed, both maximum amplitude and area of defects are quite well estimated with respect to their nominal values for the three defects in the part. However, a further investigation of these inspection results can be made to assess similarity between distance distributions of estimated versus nominal defects.

3. Assessing the robustness of our CAI method based on ASME V&V recommendations

3.1. ASME recommendations for verification and validation

As introduced, all computational methods, among which CAI, include uncertainties and numerical errors that justify applying *Verification and Validation* (V&V) recommendations. A broad investigation of the application and theory of V&V in computational engineering is presented in [20-22]. Traditional validation activities qualitatively measure the discrepancy through visual inspection of graphic plots between prediction and observation datasets [23], wherein uncertainties in the models are not taken into account. However, several disciplines, such as fluid and solid mechanics, have developed and applied systematic, rigorous and disciplined approaches for verifying and validating computational models in order to assess their prediction accuracy. For example, guides for V&V of computational solid mechanics [23], fluid dynamics [24], heat transfer [25] and material engineering [26] have already been published. Verification is defined as a process of determining how accurately a computational model represents the underlying mathematical model and its solution, while validation is defined as the process of determining the degree to which a model is an accurate representation of the real world. It is also stated that, in a V&V implementation, code verification must always precede its validation. This ASME standard concludes that system response features, validation testing and accuracy requirements are key elements of a V&V method in which the acceptable agreement for the predictive capability of the computational model is demonstrated by comparing its features of interest (validation metrics) with respect to the real model in its intended use.

In [27, 28] an overview of model validation metrics is presented as a quantitative measure of agreement between a predictive model and physical observation (measurements). In these references, a set of desired features that model validation metrics should process are highlighted and the validation metrics are categorized as hypothesis testing-based and distance-based. In [29], validation metrics are described by comparing the probability distributions of random variables representing the prediction and relevant observations. This comparison can be limited to assessing the difference between mean values of distributions or can be pushed further on comparing statistical shapes (behavior) of distributions for achieving a more detailed validation of the model. In order to perform this detailed comparison between statistic distributions, a test of significance from the hypothesis testing theory is applied. This test can be made through a comparison between cumulative distribution functions (CDFs) of estimated and actual results at a specific significance level. Two hypotheses are considered for such a hypothesis test: a null hypothesis (H_0) against an alternative hypothesis (H_A). If CDFs of estimated and actual results are sufficiently close at a specific significance level, the test results in “we cannot reject H_0 ”. This means that the result only suggests that there is not sufficient evidence against H_0 , at the significance level, in favor of H_A . This does not necessarily mean that the null hypothesis is true. In contrast, the hypothesis test results in “reject of H_0 ” when the CDFs of estimated and actual results are not sufficiently close at the significance level. The significance level in hypothesis testing, referred to as α , is defined as the probability of rejecting H_0 when it is actually true, which is also known as “Type I” error (error α) in these tests. Moreover, a confidence level in hypothesis testing, defined as $(1 - \alpha)$, is the probability of accepting a null hypothesis while it is actually false. The confidence level defines a critical region, namely a confidence interval, in which a test can face a “Type II” error (error β). Specifying a lower significance level in a test reduces the chance of rejecting a valid null hypothesis, which reduces consequently the error “Type I”. In other words, a lower significance level increases the probability of accepting an invalid null hypothesis, which increases consequently the error “Type II” [23, 27, 30, 31]. Several research work, in various engineering fields such as structural dynamics [32], steady and transient heat conduction and shocks [33], thermal decomposition of polyurethane foam [34, 35] and sheet metal forming processes [36] have already considered validation metrics applied to numerical calculations, based on this type of statistical hypothesis testing for ASME V&V recommendations.

The hypothesis testing is extended to measure differences between empirical and prediction CDFs by applying fit tests such as the Anderson–Darling (A-D) test, the Kolmogorov–Smirnov (K-S) test, the Cramer–von Mises (C-vM) test, etc. [23, 37-39]. The K-S test [40, 41] used in this paper, is based on the maximum difference between empirical and hypothetical CDFs. It is a nonparametric test, which means that sampling distributions introduced in the test do not depend on any distribution parameters (imposed type of distribution, mean value, standard deviation, etc.).

The robustness of a computational model is related to its ability to provide satisfying results, which is also assessed by ASME V&V recommendations in this work, despite the presence of slight errors in the input data. In

CAI, these errors principally originate from measurement noise that is inherent to optical and laser data acquisition tools. This means that the robustness of CAI methods should be studied with respect to scanning device noise [42, 43]. A 3D scanner analyzes extracts, from a real-world object, scan data about the shape of this object. This data is translated into triangulated 3D models and consequently, a noisy data acquisition takes the form of noisy triangulations. Errors found in scanning device triangulations can originate from a systematic bias, due to an improper calibration of the device, and/or from random errors (noise) due to ambient light and characteristics of surfaces on which scan data is obtained, such as light refraction, reflectiveness, and transparency. As illustrated in [44], during 3D data acquisition, the length of measurement ray is elongated along the direction of the ray, due to beam reflection and propagation in diverse directions, which results in higher noise along the light beam than in along transverse directions. Although the noise distribution of a real scanner is not strictly Gaussian [42], experimental measurement of noise is often assumed to be Gaussian in many disciplines [44, 45]. Since a Gaussian noise gives low weight to outliers, the effect of noise amplitude is analyzed by changing the standard deviation of noise distribution. In this work, synthetic Gaussian noise with increasing amplitude is added to the scan model to assess the effect of noise amplitude on the estimation of defects.

In the next section, K-S test is applied to develop a validation metric to assess the ability of our method in defect identification. This ability is investigated for different amplitudes of noise, which allows validating robustness of our automated inspection method.

3.2. Verification and validation methodology for CAI

Based on metrology standards, during an inspection, interest is put on estimating the magnitude of defects in a part. As introduced in section 2, we have developed an automated CAI method that is specifically focused on inspecting non-rigid parts in a free state. This method has already been presented in a previous paper [12], along with its verification. In [12], this verification has been performed through studying the application of this approach to different types of defects. Thus, our computation code related to mesh modification (incremental point insertion into CAD and scan meshes), discretized principal curvature estimation and discretized Euclidian distances assessment (between CAD and scan meshes) have been verified and details can be found in [12]. Meanwhile, the effect of mesh size on the accuracy of generating corresponding sample points with GNIF, and the effect of mesh size on filtering these sample points based on curvature criterion have also been studied. It has been observed that refined meshes lead to a better assessment of geodesic distances (using *fast marching* [17]) and also to a better assessment of principal curvatures on the discretized surfaces of CAD and scan models, which results in a better assessment of the magnitude of defects.

As introduced in section 2, the magnitude of a defect i is basically represented by its maximum amplitude (D_i^{max}) and its area (A_i). So, a first validation of the method proposed can be done directly on these metrics [12]. However, a deeper investigation of inspection results can be made. It consists in assessing how accurately the CAI process is generally able to evaluate the distance distribution of defects. The distance distribution of a defect in a CAI is defined as the Euclidean distance value assigned to a set of nodes located on the identified defect of scan mesh wherein the Euclidean distance between the scan model and deformed CAD model (after FENR) exceeds the tolerance value. Since the nominal distance distribution of defects is known, we can compare the estimated distance distribution of defects with the nominal ones to investigate the estimated inspection results. As introduced in the previous paragraphs, this comparison can be made based on V&V recommendations and tools. We propose in this paper a validation metric that is intended to compare estimated defects versus nominal defects. As introduced in Section 2 (see Figure 5), maximum amplitude D_i^{max} and area A_i of defects, on a given manufactured part, are identified with respect to engineering tolerances. These characteristics of defects are obtained from Euclidean distance distributions between scan and CAD models. These distributions are computed as discrete Euclidean distances at each node of the scan mesh and then a continuous distribution is calculated by interpolating these discrete distance across triangles of the scan mesh. A defect is basically defined as a zone for which the actual manufactured part, once FENR applied, deviates from the specified geometry (outside the tolerance zone).

In this study, scan models are simulated by adding defect (e.g. bumps) in CAD models, which is followed by applying an elastic deformation due to gravity and residual stress effects in free-state. By doing that (considering simulated defects) the distance distribution of defects, as estimated with our method, can be easily compared with the nominal distance distribution of defects, since it is known. The example introduced in section 2 (see Figure 6-a) features 3 bumps. Figure 8 presents, for these 3 bumps, a visual comparison between nominal and estimated identified defects.

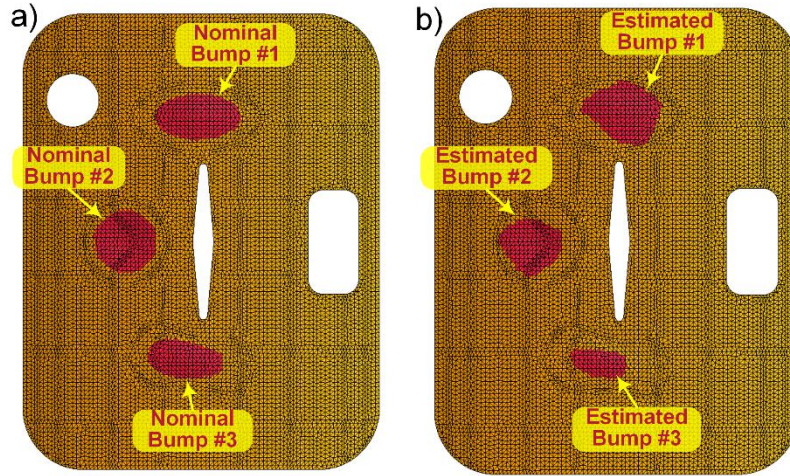


Figure 8: defects are identified as red zones based on the tolerance value (0.4 mm) a) for nominal defects b) for estimated defects.

The comparison between nominal and estimated defects is performed using a statistical validation method as presented in Section 3.1. It is based on ASME V&V recommendations and on the K-S test. The result of a K-S test at a given significance level is provided as a p-value that is calculated between two data sets (the two data sets and their sizes are referred to as n and n'). This p-value is related to K-S statistic, which is the maximum distance ($S_{n,n'}$) between CDFs of the two data sets, and to sizes of the 2 data sets. The p-value can be interpreted as a measure of plausibility of the null hypothesis (H_0). This means that if the K-S test results in a p-value that is higher than the significance level considered, “we cannot reject H_0 ”. In our case, the 2 data sets that are compared with a K-S test are the distance distributions (between CAD and scan models) associated with nominal defects and respective estimated defects. Note that this comparison is performed defect by defect and not globally. Therefore, the null hypothesis for a K-S test is that the distance distributions associated with nominal and estimated defects are sufficiently similar. In general, supposing the size of sample data stays approximately unchanged, the probability of rejecting the null hypothesis increases when the maximum distance between CDFs of the two data increases. As a consequence, a K-S test will result in a lower p-value when $S_{n,n'}$ increases. This can be observed in Figure 9 where a comparison is presented between the CDFs of nominal and estimated defects for Bump #1 and Bump #2 as defined in the example introduced above (Figure 6-a). It can be visually observed in Figure 8 that distance distributions of nominal and estimated defects for Bump #2 are likely to be more similar to each other than for Bump #1. This is reflected in the result of K-S test at 5% of significance level as presented in Figure 9. Indeed, for Bump #1 p-value is 0.000 (with $n = 180, n' = 192, S_{n,n'} = 0.211$) while for Bump #2 p-value is 0.356 (with $n = 195, n' = 157, S_{n,n'} = 0.098$). In this case, the result of the K-S test is that H_0 can be rejected for Bump #1 and that H_0 cannot be rejected for Bump #2.

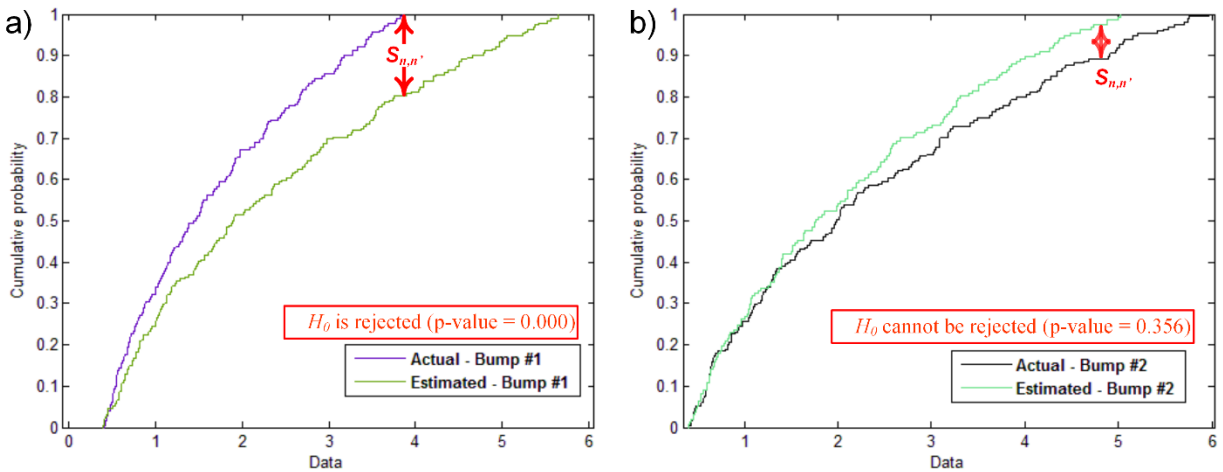


Figure 9: CDF for nominal and estimated defects for Bump #1 and Bump #2.

As introduced previously, validation tests on distance distributions (between CAD and scan data) associated with each defect are performed as a comparison between the distance distribution of the nominal defect (Dd_a) and the distance distribution of the estimated defect as identified (Dd_e). Dd_a is calculated on the set of nodes associated

with the nominal defect on the scan mesh before adding the flexible deformation (shown as purple dots in Figure 10-a). Dd_e is calculated on the set of nodes associated with the estimated defect as identified, on the scan mesh in a free-state (shown as red dots in Figure 10-b, c, and d). Subsequent comparisons are made, based on applying a K-S test on these two distance distributions. The distance distribution of a defect is well estimated or validated when this K-S test shows satisfying results (example shown in Figure 10-b). When it is the case, enough sample points have been removed but not too many. Indeed, if too many sample points are removed, deformation in free-state is likely to be badly captured in FENR. In Figure 10-c, the deformed CAD model (after FENR) does not follow accurately enough the flexible deformation of the scan model in free-state because too many sample points have been removed. This results in overestimating the defect. In this case, K-S test (Figure 10-b) will tend to “reject H_0 ”. In Figure 10-d, due to in-plane GNIF errors and to not removing enough sample points, CAD sample points are pushed to the defect shape. This leads to badly estimating the defect, but the result of K-S test associated with Figure 10-d depends on the location of falsely remaining sample points after filtering. If falsely remaining sample points are close to the tip of defect, the K-S test is likely to tend to “reject H_0 ”. On the contrary, if these falsely remaining sample points are far from the tip of defect, the distance distribution of estimated defect can still be statistically similar to the nominal one, wherein the K-S test is likely to tend to “cannot reject H_0 ”.

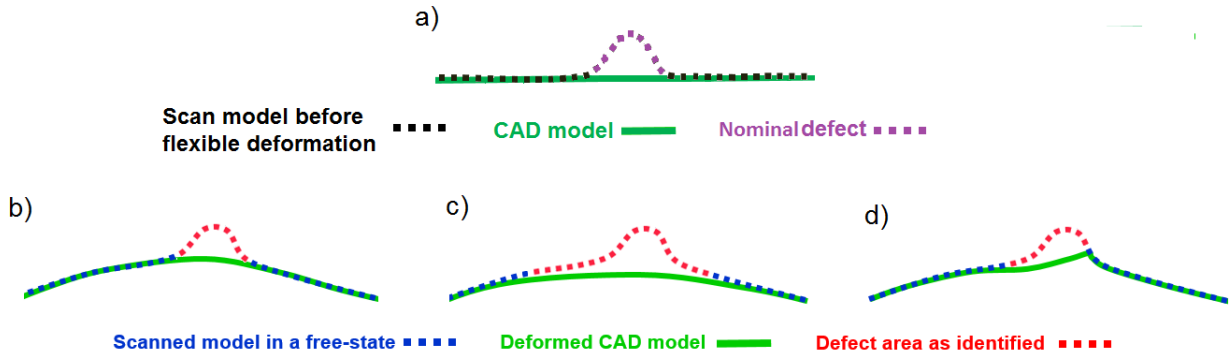


Figure 10: Estimation of the distance distribution of a defect a) nominal defect, b) for an accurate inspection c) for an overestimated defect d) for a badly estimated defect.

3.3. Robustness of our CAI method

As mentioned above, synthetic noise is added to the simulated scan data. This is aimed at replicating the actual noise that cannot be avoided in real scan data during the scanning (digitization) process. Since this noise is synthetic, various amplitudes and distributions of noise can be considered, which allows assessing the robustness of our automatic fixtureless inspection method for non-rigid parts. Synthetic noise applied is Gaussian and since the magnitude of noise for optic and laser scanners is much higher along the beam direction, this synthetic noise is added as random numbers to node coordinates of the scan mesh in the normal direction (perpendicular to the surface). These random numbers are generated as Gaussian distributions with null mean values ($\mu = 0$) and with three different standard deviations (σ): 0.01, 0.02 and 0.03 mm. In order to keep the magnitude of noise in a reasonable range with respect to tolerances, these random numbers are taken in the $[-2 \times \sigma, 2 \times \sigma]$ interval for a given standard deviation (σ). For the part introduced in Figure 6-a, 4 scan models are presented and compared in Figure 11 with various amplitudes of noise.

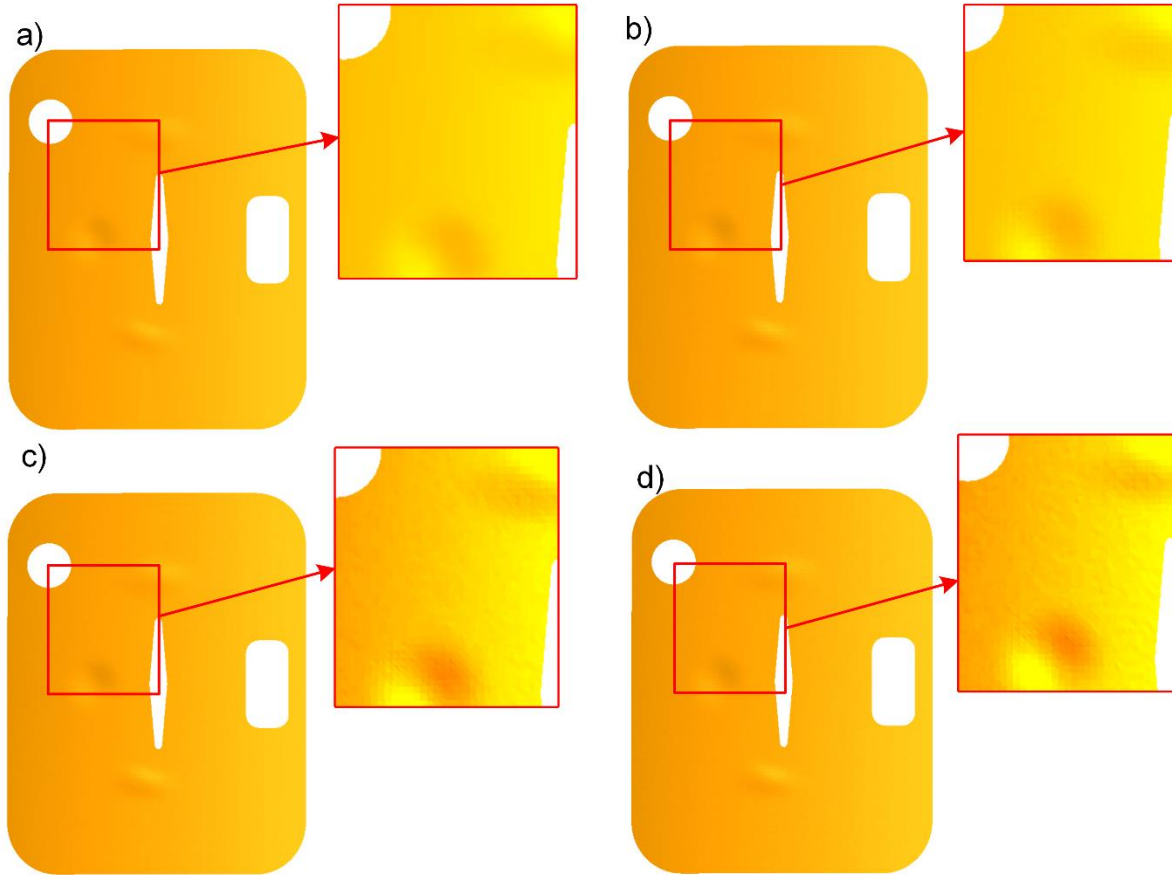


Figure 11: a) a noise-free scan mesh b), c), d) scan meshes with synthetic noise with Gaussian distribution with zero mean value and standard deviation equal to b) 0.01mm c) 0.02mm d) 0.03mm.

The model shown in Figure 11-a is noise-free while the models shown in Figure 11-b, Figure 11-c, and Figure 11-d were respectively generated using standard deviations equal to 0.01, 0.02 and 0.03 mm. we can visually observe that a noise-free scan mesh has a much smoother mesh surface if compared to a noisy scan mesh.

In the next section, our automatic and fixtureless CAI method for non-rigid parts is applied and validated in several cases. These cases consider 2 different parts with, for each part, different types and distributions of defects, different deformations associated with the free-state and different amplitudes of noise.

4. Validation results for cases with small free-state deformation

4.1. Validation cases considered

In this section, the robustness of our automatic and fixtureless CAI method is validated on two aluminum parts (referred to as part A and part B). Part A is the part introduced in Figure 2 and part B is a second non-rigid part, which is also typical of non-rigid parts used in the aerospace industry (see Figure 16). As explained in section 2, scan models used as validation cases in this article are simulated by deforming CAD models via FEA and by adding geometrical deviations (defects). To this end, one single free-state deformation (referred to as bending) is applied on part A while two free-state deformations are considered for part B (referred to as bending and torsion). For both parts, as illustrated in Figure 12, small (local) and big (global) defects are considered. For each validation case, the robustness of our inspection method is studied by applying synthetic noise, as introduced above. Since defects are a priori known for all case studies considered, comparisons can be made between size, area and distance distributions of estimated defects in comparison with nominal defects.

For maximum amplitude and area of defects, absolute (in mm) and relative (in percentage) error between estimated and nominal sizes of defects are calculated for each case, using:

$$\text{Absolute error (mm)} = (\text{estimated size}) - (\text{nominal size}) \quad \text{Equation (1)}$$

$$\text{Relative error (\%)} = \frac{(\text{estimated size}) - (\text{nominal size})}{(\text{nominal size})} \times 100 \quad \text{Equation (2)}$$

Therefore, in results presented below, for both maximum amplitude and area of defects, negative error values represent an underestimation of defects and positive error values an overestimation of defects.

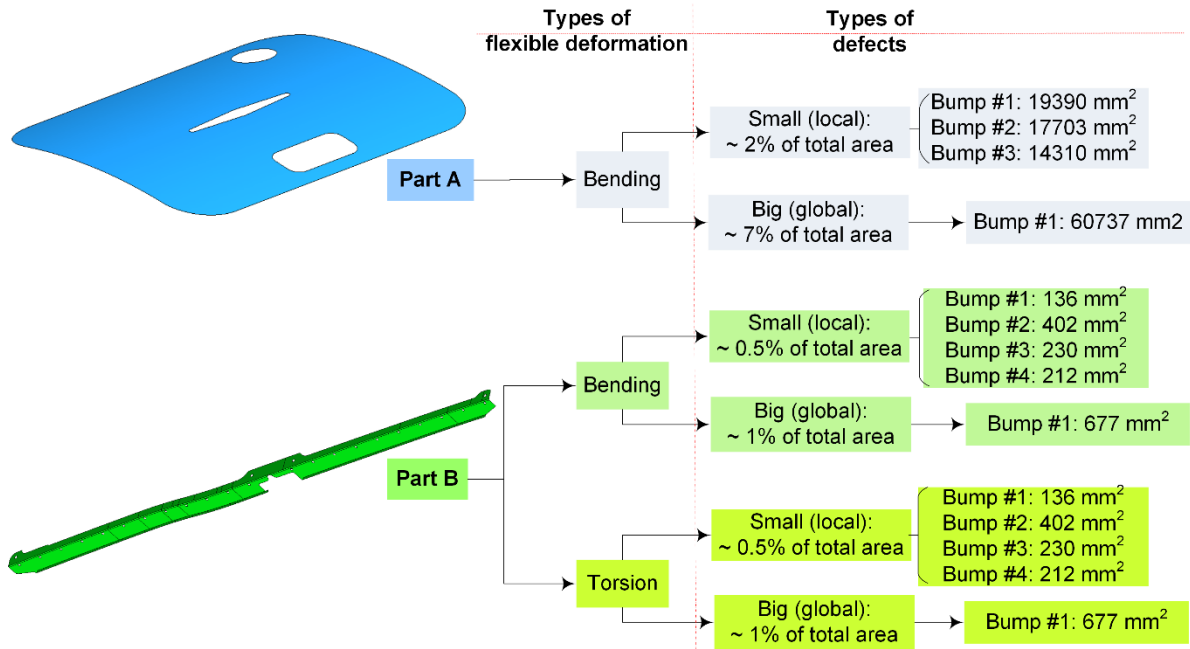


Figure 12: Synthesis of validation cases with small free-state deformation

We have successfully implemented our automated and fixtureless CAI method and its validation using several tools. GNIF calculations are carried out using a MATLABTM code to generate sets of corresponding sample points. The generation of around 500 corresponding sample points, with this code, takes approximately 8 minutes on a computer equipped with an Intel^(R) CoreTM i7 at 3.60 GHz with 32 GB RAM. Mesh generation, mesh transformation, discrete curvature calculations, FEA non-rigid registration and Euclidean distance calculations between deformed CAD and scan data are performed using the research platform developed by our research team [46]. This platform is based on C++ code, on Open CASCADETM libraries for geometry and on Code_AsterTM as FEA solver. We also use GmshTM [47] for visualizing 3D models and distance distributions. Sample points filtering takes around 2 minutes for a CAD mesh featuring 10545 nodes on a computer with specifications as mentioned above. Finally, the K-S tests are performed in a negligible CPU time by applying MATLABTM (using *kstest2*) to validate the distance distribution of estimated defects.

4.2. Results for part A

The first model, referred to as part A, is shown in Figure 2 and Figure 13. This part is approximately 1100 mm long, 860 mm wide and 3 mm thick with 879067 mm² area. The scan model associated with this model in free-state is simulated using a bending deformation for which maximum displacement is approximately 10 mm. Thus, if compared to the part dimensions (1100 mm length) this state of deformation is consistent with a small displacement assumption.

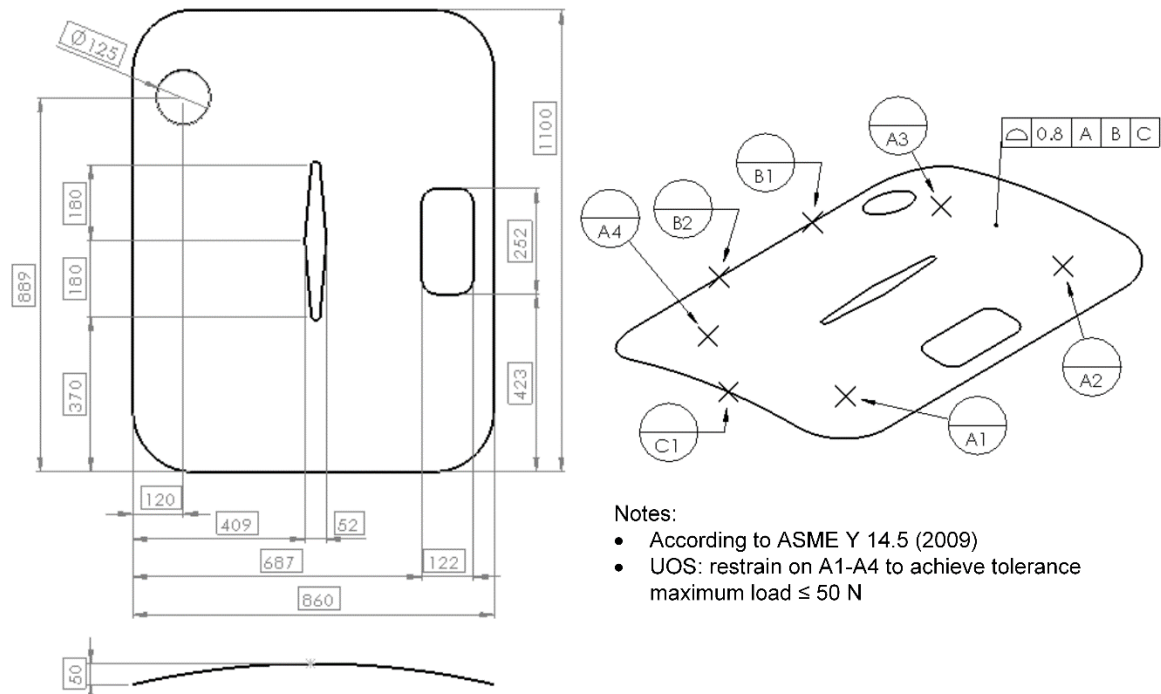


Figure 13: CAD model along with GD&T specification for part A (dimensions are in mm).

Depending on the case considered, the scan model of part A features two types of defects, small (local) (see Figure 6-a) or big (global) defects (see Figure 15-a). The distance distribution related to the nominal size of defects for part A, with small (local) defects, is presented in Figure 14-a. Estimated inspection results, as distance distributions, are illustrated with noise-free and different noisy scan meshes in Figure 14-b, c, d and e wherein the noise amplitude are increasing (as mentioned previously for a noisy scan model with a standard deviation of 0.01, 0.02 and 0.03 mm respectively). It is worth noting that the flexible deformation and the nominal size of defects are the same for all noise-free and noisy scan meshes. Results obtained with our automatic fixtureless CAI method (maximum amplitude and area of defects) are summarized in Table 1. These results show that the estimation of maximum amplitude is better for Bump #2 than for Bump #3 and especially for Bump #1. This can be explained considering that the shape of defects is affected by flexible deformation in FENR. This effect depends on the nature and magnitude of flexible deformation and on the type and dimensions of defects. Indeed, if flexible deformation in the vicinity of a given defect is high and if the defect itself is quite flexible, this may affect the shape of the defect. Flexible deformation across the scan model in the vicinity of Bump #1 and #3 is comparatively larger if compared to that of Bump #2. In fact, the scan model simulates the part in a free-state for which the central zone of the part is constrained on an inspection table. Therefore, flexible deformation of the part is smaller in the center and grows towards exterior borders of the part. Regarding the estimation of defects area, these results show that area is well estimated for Bump #1 and is reasonably estimated for Bump #2. These results also show that the presence of noise as well as increasing the amplitude of noise has not a very significant effect on the estimation of maximum amplitude and area of defects. It is also observed that, in some cases, the presence of scanning noise improves the estimation of defects size. This phenomenon can be explained considering that scanning noise is randomly distributed over the surface of the scan mesh. Since our CAI approach aims at filtering out sample points around defect zones, the presence of noise in the vicinity of sample points that are close to defect zones may result in filtering these sample points based on curvature and stress criteria. In fact, these scanning outliers may locally bring about high curvature and/or stress values that surpass the thresholds of sample point filtering criteria. Therefore, in some cases, the presence of noise on/around defects may improve removing irrelevant sample points close to defect zones. As introduced in section 3.2, the robustness of our method is validated by applying K-S test for distance distribution of defects as identified (Table 2) using the K-S test on these inspection results. The K-S test results presented in this paper are illustrated with colors (green for “ H_0 cannot be rejected”, red for “ H_0 is rejected” and brown for “ H_0 is borderline”). Results presented in Table 2 globally show that, according to the V&V process presented in this paper, distance distributions for Bump #2 and Bump #3 are considered as sufficiently similar to the nominal distance distributions, at a 5% significance level, which is not the case for Bump #1. As explained in section 3.2, for Bump #1, too many sample points are filtered out close to the defect (see Figure 4-b), which implies that the deformed CAD model cannot accurately fit free-state deformation of the scan model. This leads to overestimating the maximum amplitude of this defect. A source of error that affects the distance distribution associated with estimated defects is indeed a significant bias in the generation of sample points with the GNIF

method. This bias in GNIF comes from significant inaccuracies in the calculation of geodesic distances with the fast marching algorithm [17]. Inaccurate geodesic distances indeed result in inaccuracy in the in-plane location of sample points generated by GNIF. Error in the in-plane location of these sample points causes non-realistic stretching in FENR, which is a source of inaccuracy in inspection results.

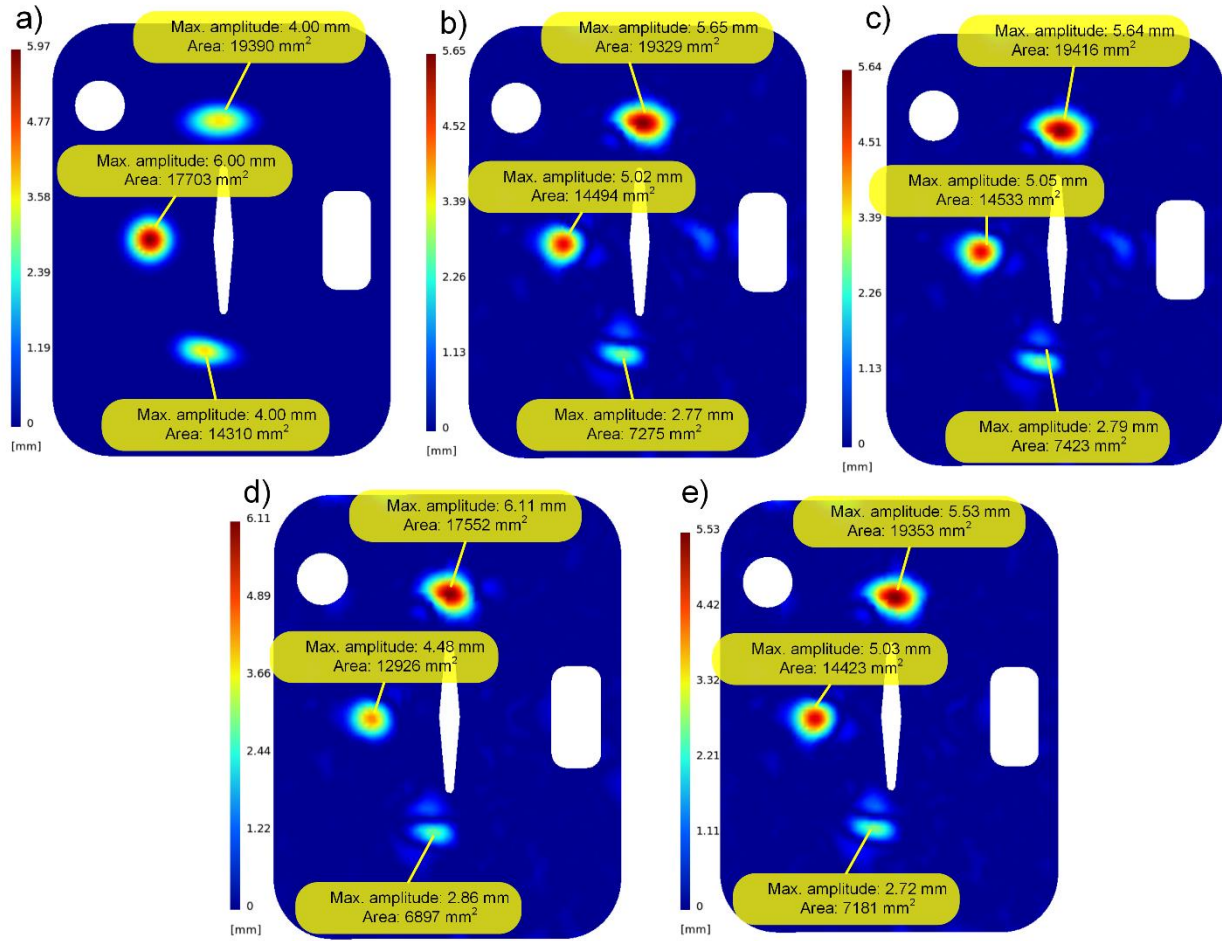


Figure 14: a) nominal defect distance distribution for part A with small (local) defects, comparison between the CAD and scan model of part A with small (local) defects and bending deformation as a distance distribution for b) noise-free scan mesh c) noisy scan mesh with $\sigma=0.01$ mm d) noisy scan mesh with $\sigma=0.02$ mm e) noisy scan mesh with $\sigma=0.03$ mm.

Table 1: Estimated size of defects and errors for part A with small (local) defects and bending deformation.

		Maximum amplitude of defects (D_i^{max})				Area of defects (A_i)			
		Nominal [mm]	Estimated [mm]	Absolute error [mm]	Error [%]	Nominal [mm ²]	Estimated [mm ²]	Absolute error [mm]	Error [%]
BUMP #1	Noise-free	4.00	5.65	1.65	41.16	19390	19329	-61	-0.31
	$\sim N(0, \sigma = 0.01)$	4.00	5.64	1.64	41.08	19390	19416	26	0.13
	$\sim N(0, \sigma = 0.02)$	4.00	6.11	2.11	52.71	19390	17552	-1838	-9.48
	$\sim N(0, \sigma = 0.03)$	4.00	5.53	1.53	38.24	19390	19353	-37	-0.19
BUMP #2	Noise-free	6.00	5.02	-0.98	-16.33	17703	14494	-3209	-18.13
	$\sim N(0, \sigma = 0.01)$	6.00	5.05	-0.95	-15.78	17703	14533	-3170	-17.91
	$\sim N(0, \sigma = 0.02)$	6.00	4.48	-1.52	-25.33	17703	12926	-4777	-26.98
	$\sim N(0, \sigma = 0.03)$	6.00	5.03	-0.97	-16.10	17703	14423	-3281	-18.53
BUMP #3	Noise-free	4.00	2.77	-1.23	-30.75	14310	7275	-7035	-49.16
	$\sim N(0, \sigma = 0.01)$	4.00	2.79	-1.21	-30.34	14310	7423	-6887	-48.12
	$\sim N(0, \sigma = 0.02)$	4.00	2.86	-1.14	-28.50	14310	6897	-7413	-51.81
	$\sim N(0, \sigma = 0.03)$	4.00	2.72	-1.28	-32.00	14310	7181	-7129	-49.82

Table 2: Validation results with K-S tests (H_0 : the distance distribution of nominal and estimated defects are sufficiently similar) at 5% significance level for part A with small (local) defects and bending deformation

		p-value
BUMP #1	Noise-free	0.000
	$\sim N(0, \sigma = 0.01)$	0.000
	$\sim N(0, \sigma = 0.02)$	0.000
	$\sim N(0, \sigma = 0.03)$	0.001
BUMP #2	Noise-free	0.356
	$\sim N(0, \sigma = 0.01)$	0.376
	$\sim N(0, \sigma = 0.02)$	0.039
	$\sim N(0, \sigma = 0.03)$	0.293
BUMP #3	Noise-free	0.144
	$\sim N(0, \sigma = 0.01)$	0.141
	$\sim N(0, \sigma = 0.02)$	0.235
	$\sim N(0, \sigma = 0.03)$	0.090

H_0 is rejected
 H_0 cannot be rejected
 H_0 is borderline

In the following paragraph, as presented in Figure 12, another validation case is applied on part A. The difference with previous cases is about defects. For this new case, scan data includes a big (global) defect instead of three small (local) defects. The nominal size of this defect is illustrated, as a distance distribution, in Figure 15-a. It is compared with results provided by our automatic fixtureless CAI method with bending deformation in Figure 15-b for noise-free scan data. Inspection results for noisy scan meshes (with $\sigma = 0.01, 0.02$ and 0.03 mm) are also shown respectively in Figure 15-c, d, and e. Maximum amplitude and area of estimated defects along with the relative error with respect to the nominal size of defect are summarized in Table 3. Like in the previous case for this part, these results show that the defect size is reasonably well estimated, and that noise does not seem to have a clear effect and a potential worsening of estimation results. As observed for Bump #2 in the previous case for part A, the size of defect in this case is also well estimated since the flexible deformation of part in the vicinity of this defect is comparatively small.

As for small (local) defects, the validation of these results based on K-S test at a 5% significance level, for distance distribution of defects as identified is presented in Table 4. In this case, V&V results show that the distance distribution of the estimated defect is sufficiently similar to the nominal defect at a 5% significance level.

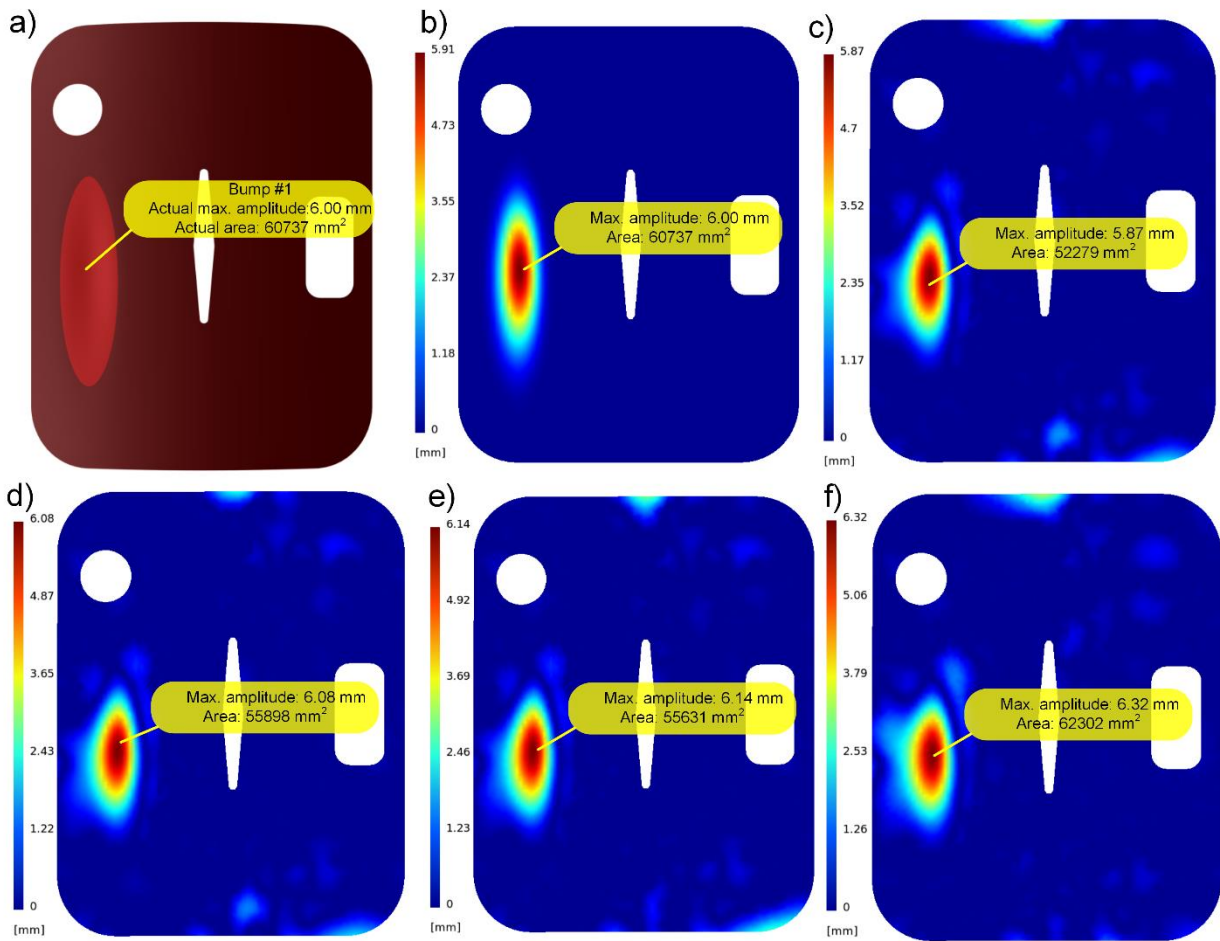


Figure 15: a) the scanned part with the nominal dimensions of big (global) defect b) nominal defect distance distribution for part A with a big (global) defect, comparison between the CAD and scan model of part A with a big (global) defect and bending deformation as a distance distribution for c) noise-free scan mesh d) noisy scan mesh with $\sigma=0.01$ mm e) noisy scan mesh with $\sigma=0.02$ mm f) noisy scan mesh with $\sigma=0.03$ mm.

Table 3: Estimated size of defects and errors for part A with a big (global) defect and bending deformation.

		Maximum amplitude of defects (D_i^{max})				Area of defects (A_i)			
		Nominal [mm]	Estimated [mm]	Absolute error [mm]	Error [%]	Nominal [mm ²]	Estimated [mm ²]	Absolute error [mm]	Error [%]
BUMP #1	Noise-free	6.00	5.87	-0.13	-2.16	60737	52279	-8458	-13.93
	$\sim N(0, \sigma = 0.01)$	6.00	6.08	0.08	1.41	60737	55898	-4839	-7.97
	$\sim N(0, \sigma = 0.02)$	6.00	6.14	0.14	2.40	60737	55631	-5106	-8.41
	$\sim N(0, \sigma = 0.03)$	6.00	6.32	0.32	5.37	60737	62302	1565	2.58

Table 4: Validation results with K-S tests (H_0 : the distance distribution of nominal and estimated defects are sufficiently similar) at 5% significance level for part A with a big (global) defect and bending deformation.

		p-value
BUMP #1	Noise-free	0.755
	$\sim N(0, \sigma = 0.01)$	0.865
	$\sim N(0, \sigma = 0.02)$	0.930
	$\sim N(0, \sigma = 0.03)$	0.414

■ H_0 is rejected
■ H_0 cannot be rejected
■ H_0 is borderline

4.3. Results for part B

Next validation cases are intended to validate the robustness of our automatic fixtureless inspection method for non-rigid parts on a more featured type part (referred to as part B in Figure 12). This part, shown in Figure 16, is a long part which is also inspired from parts used in the aerospace industry. It features more details and smaller features as well as higher curvature in some locations. This part, made of aluminum, is approximately 1150 mm long and dimensions of the U channel are approximately $20 \times 40 \times 7$ mm with 1 mm thickness. As synthesized in Figure 12, two types of defects (small (local) and big (global)) are applied on this part as well as two types flexible deformation in a free-state. One is referred to as bending deformation (Figure 17a) and the other one as torsion deformation (Figure 17b). In both cases, these free-state deformations are consistent with a small displacement assumption.

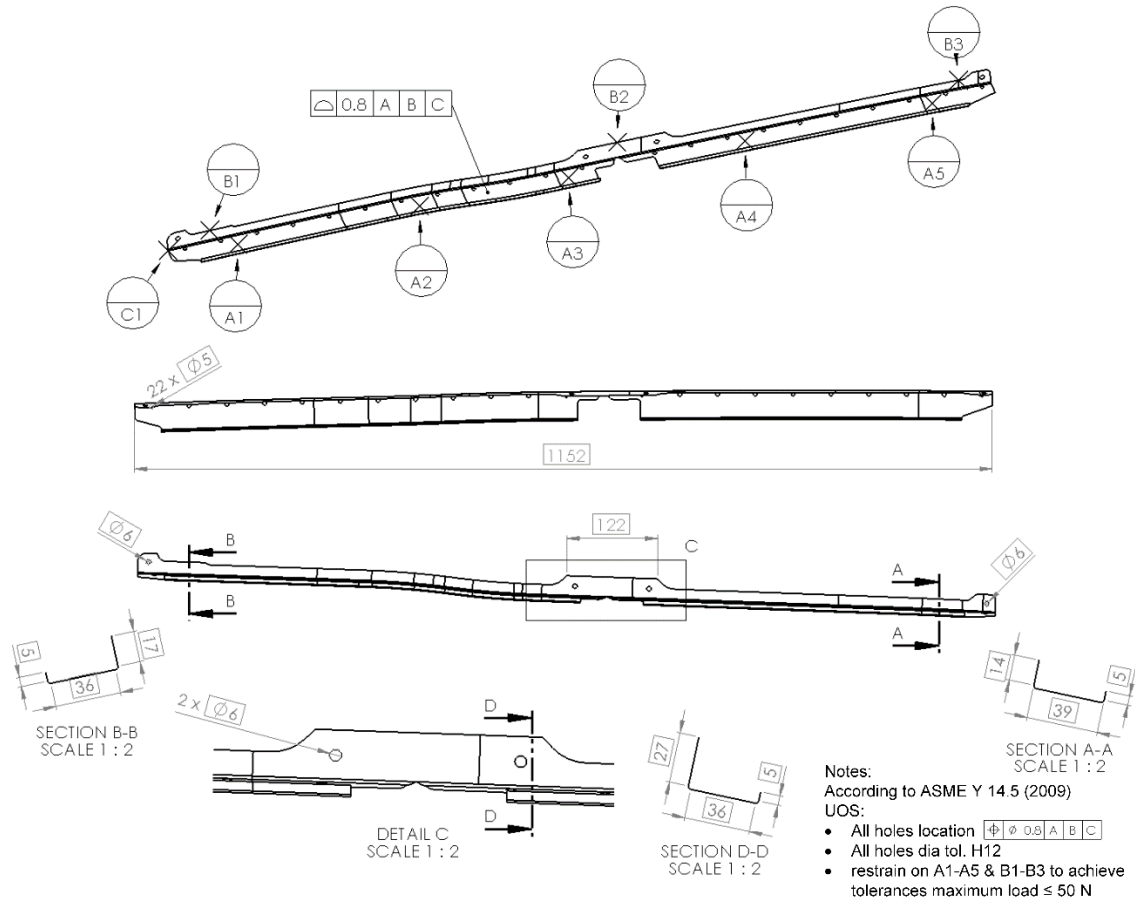


Figure 16: CAD model along with GD&T specification for part B (dimensions are in mm).

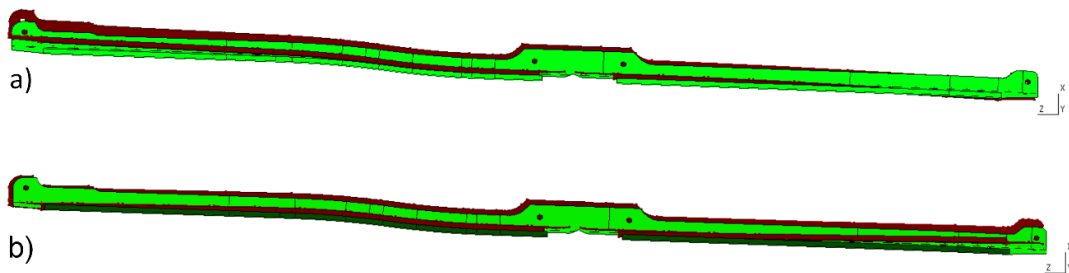


Figure 17: Side views of the CAD model for part B (in green) compared with scan data in a free-state (in brown) with a) bending deformation b) torsion deformation.

In the first validation case for part B, the flexible deformation of the scan model in a free-state is simulated by bending, and four small (local) bump defects are applied. The nominal size of defects (amplitude and area) for this case are presented in Figure 18-a. The nominal size of defects is compared with results provided by our automatic fixtureless CAI method with bending deformation in Figure 18-b for noise-free scan data. Inspection results for noisy scan meshes (with $\sigma = 0.01, 0.02$ and 0.03 mm) are also shown respectively in Figure 18-c, d, and e.

Maximum amplitude and area of estimated defects along with the relative error with respect to the nominal size of defects are summarized in Table 5. In this case, amplitude and area of defects are estimated with reasonably good accuracy in all cases and for all defects. These results also show that noise does not have a negative effect on the estimation of defects. In some cases, noise can surprisingly even improve defect identification instead of worsening it. Validation of these results, based on K-S test at a 5% significance level, is presented in Table 7. V&V results for this case show that the distance distribution of defects is quite well estimated at a 5% significance level.

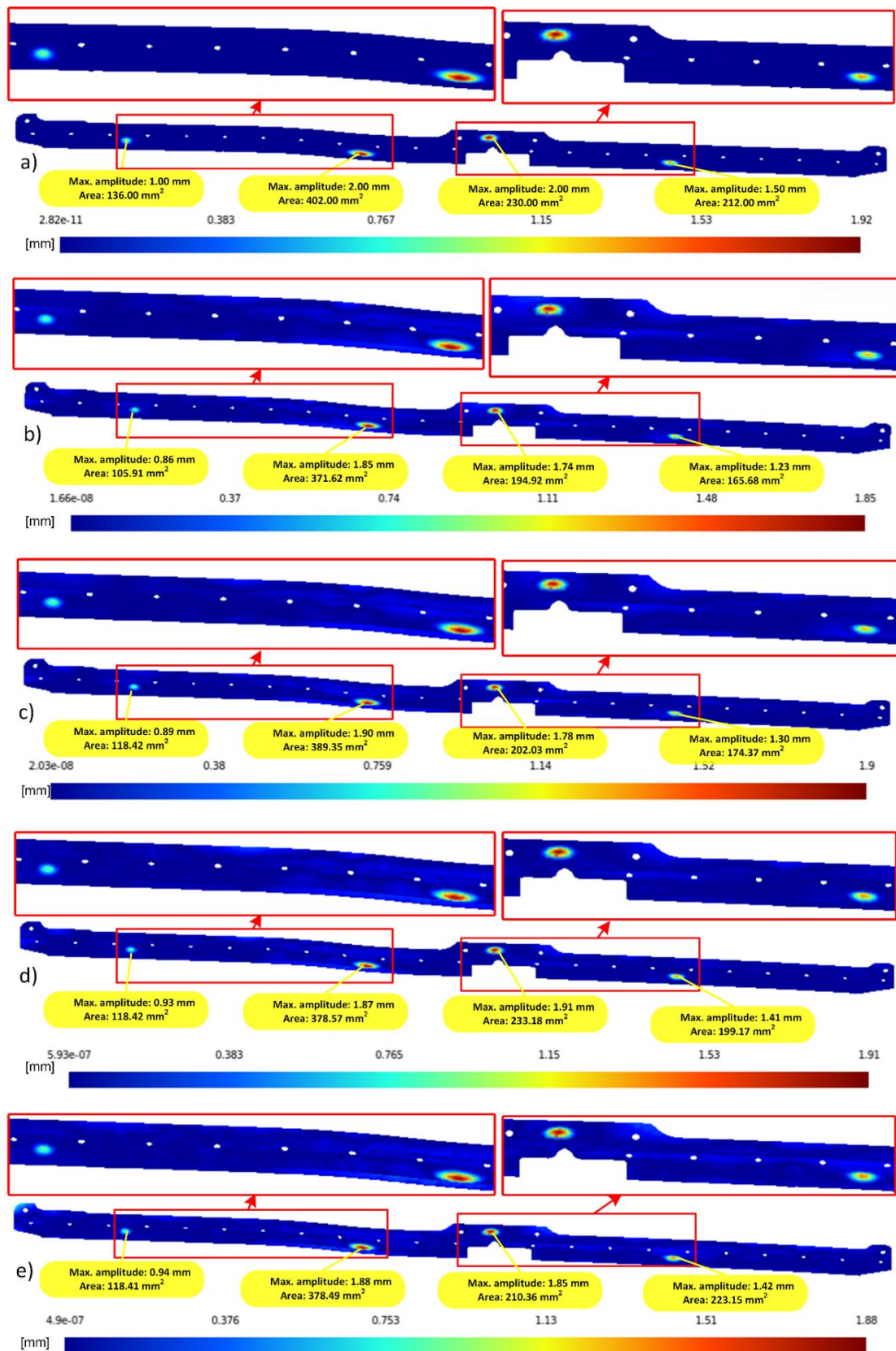


Figure 18: a) nominal defect distance distribution for part B with small (local) defects, comparison between the CAD and scan model with small (local) defects and bending deformation as a distance distribution for b) noise-free scan mesh c) noisy scan mesh with $\sigma=0.01$ mm d) noisy scan mesh with $\sigma=0.02$ mm e) noisy scan mesh with $\sigma=0.03$ mm.

Table 5: Estimated size of defects and errors for part B with small (local) defects and bending deformation.

		Maximum amplitude of defects (D_i^{max})				Area of defects (A_i)			
		Nominal [mm]	Estimated [mm]	Absolute error [mm]	Error [%]	Nominal [mm ²]	Estimated [mm ²]	Absolute error [mm]	Error [%]
BUMP #1	Noise-free	1.00	0.86	-0.14	-14.00	136	106	-30	-22.13
	$\sim N(0, \sigma = 0.01)$	1.00	0.89	-0.11	-11.00	136	118	-18	-12.93
	$\sim N(0, \sigma = 0.02)$	1.00	0.93	-0.07	-7.00	136	118	-18	-12.91
	$\sim N(0, \sigma = 0.03)$	1.00	0.94	-0.06	-6.00	136	118	-18	-12.93
BUMP #2	Noise-free	2.00	1.85	-0.15	-7.50	402	372	-30	-7.56
	$\sim N(0, \sigma = 0.01)$	2.00	1.90	-0.10	-5.00	402	389	-13	-3.15
	$\sim N(0, \sigma = 0.02)$	2.00	1.87	-0.13	-6.50	402	379	-23	-5.83
	$\sim N(0, \sigma = 0.03)$	2.00	1.88	-0.12	-6.00	402	378	-24	-5.85
BUMP #3	Noise-free	2.00	1.74	-0.26	-13.00	230	195	-35	-15.25
	$\sim N(0, \sigma = 0.01)$	2.00	1.78	-0.22	-11.00	230	202	-28	-12.16
	$\sim N(0, \sigma = 0.02)$	2.00	1.91	-0.09	-4.50	230	233	3	1.38
	$\sim N(0, \sigma = 0.03)$	2.00	1.85	-0.15	-7.50	230	210	-20	-8.54
BUMP #4	Noise-free	1.50	1.23	-0.27	-18.00	212	166	-46	-21.85
	$\sim N(0, \sigma = 0.01)$	1.50	1.30	-0.20	-13.33	212	174	-38	-17.75
	$\sim N(0, \sigma = 0.02)$	1.50	1.41	-0.09	-6.00	212	199	-13	-6.05
	$\sim N(0, \sigma = 0.03)$	1.50	1.42	-0.08	-5.33	212	223	11	5.26

The nominal size of defects for part B with small (local) defects (Figure 19-a) is then compared with results provided by our automatic fixtureless CAI method, with torsion deformation, in Figure 19-b for noise-free scan data. Inspection results for noisy scan meshes (with $\sigma = 0.01, 0.02$ and 0.03 mm) are also shown respectively in Figure 19-c, d, and e. Maximum amplitude and area of estimated defects along with the relative error with respect to the nominal size of defects are summarized in Table 6. These results for noise-free scan mesh show that the estimation error for maximum amplitude of Bump #2 is higher than the other defects. Meanwhile, the estimation error of Bump #2, in this case, is increased compared to inspection results for the previous case. Referring to distance distribution of model in Figure 19, it can be observed that the size of Bump #2 is underestimated. This observation infers that some excessive sample points on the defect area still remains after sample points filtering process. This is due to the fact that assessing discretized principal curvatures is sensitive to mesh size. The curvature on a defect with a coarse mesh may bring about significant variation compared to the real curvature. This problem can be resolved by refining the scan mesh to assess a more realistic curvature of defect, which leads to identifying defect area and filtering out all sample points on defects. We can also observe that introducing scan noise (with $\sigma = 0.03$ mm) considerably reduces the estimation error for Bump #2. In this context, the presence of arbitrarily distributed noise close to defect area leads to a curvature outlier which helps to detect the defect and to filter out more sample points on this defect area. Like in the first case for part B, these results also show that noise does not have a negative effect on the estimation of defects and that the estimation is even improved with noise for some cases. Amplitude and area of defects are estimated with reasonably good accuracy in general with higher errors for Bump #1 and Bump #2. As for bending deformation, validation of these results, based on K-S test at a 5% significance level, are presented in Table 7. V&V results show that the distance distribution of defects zones is well estimated in all cases.

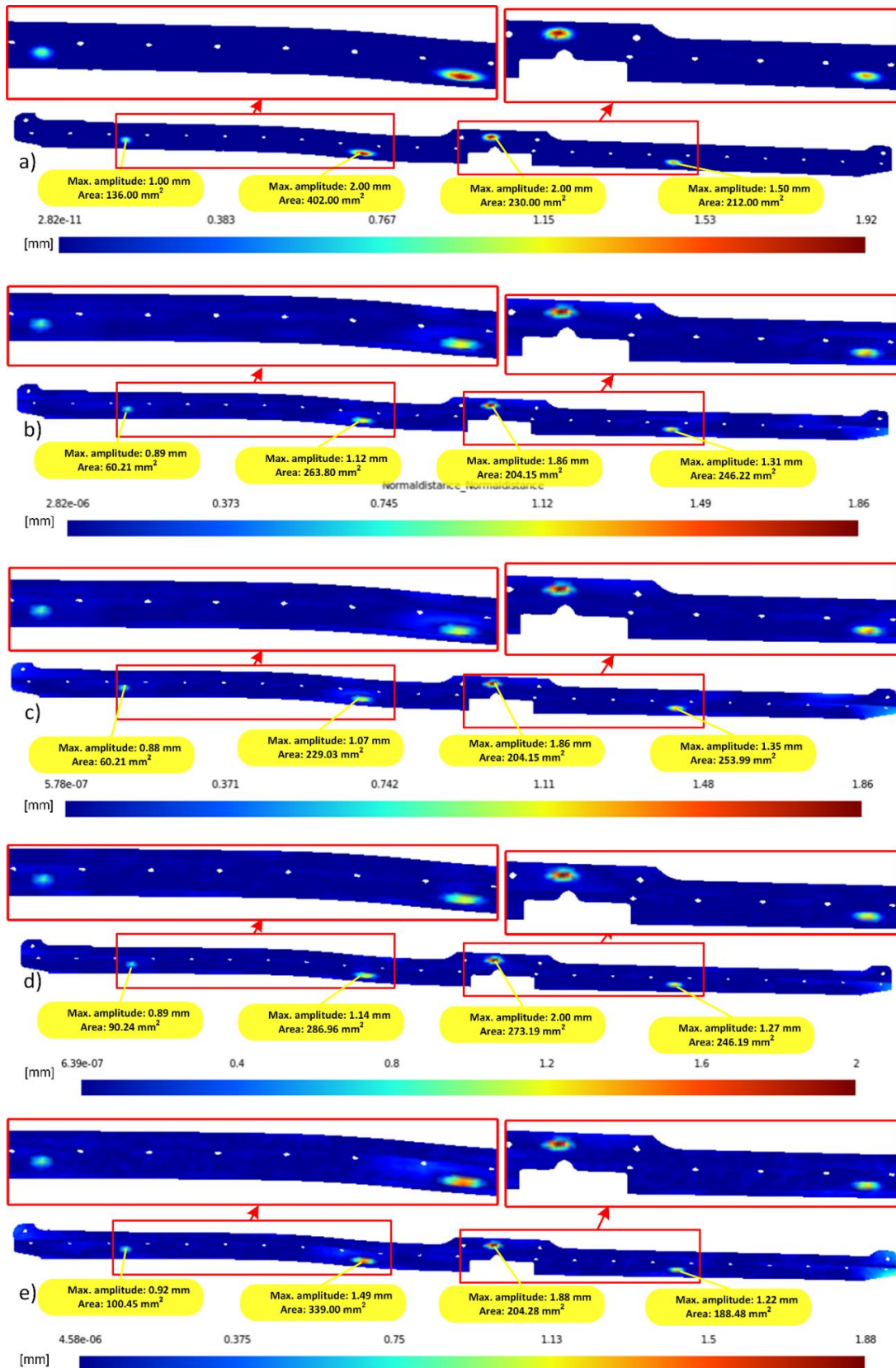


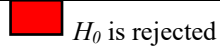
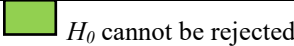
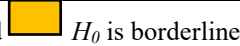
Figure 19: a) nominal defect distance distribution for part B with small (local) defects, comparison between the CAD and scan model with small (local) defects and torsion deformation as a distance distribution for b) noise-free scan mesh c) noisy scan mesh with $\sigma=0.01$ mm d) noisy scan mesh with $\sigma=0.02$ mm e) noisy scan mesh with $\sigma=0.03$ mm.

Table 6: Estimated size of defects and errors for part B with small (local) defects and torsion deformation.

		Maximum amplitude of defects (D_i^{max})				Area of defects (A_i)			
		Nominal [mm]	Estimated [mm]	Absolute error [mm]	Error [%]	Nominal [mm ²]	Estimated [mm ²]	Absolute error [mm]	Error [%]
BUMP #1	Noise-free	1.00	0.89	-0.11	-11.00	136	90	-46	-33.67
	$\sim N(0, \sigma = 0.01)$	1.00	0.88	-0.12	-12.00	136	90	-46	-33.67
	$\sim N(0, \sigma = 0.02)$	1.00	0.89	-0.11	-11.00	136	90	-46	-33.65
	$\sim N(0, \sigma = 0.03)$	1.00	0.92	-0.08	-8.00	136	100	-36	-26.14
BUMP #2	Noise-free	2.00	1.12	-0.88	-44.00	402	264	-138	-34.38
	$\sim N(0, \sigma = 0.01)$	2.00	1.07	-0.93	-46.50	402	229	-173	-43.03
	$\sim N(0, \sigma = 0.02)$	2.00	1.14	-0.86	-43.00	402	287	-115	-28.62
	$\sim N(0, \sigma = 0.03)$	2.00	1.49	-0.51	-25.50	402	339	-63	-15.67
BUMP #3	Noise-free	2.00	1.86	-0.14	-7.00	230	204	-26	-11.24
	$\sim N(0, \sigma = 0.01)$	2.00	1.86	-0.14	-7.00	230	204	-26	-11.24
	$\sim N(0, \sigma = 0.02)$	2.00	2.00	0.00	0.00	230	273	43	18.78
	$\sim N(0, \sigma = 0.03)$	2.00	1.88	-0.12	-6.00	230	204	-26	-11.18
BUMP #4	Noise-free	1.50	1.31	-0.19	-12.67	212	246	34	16.14
	$\sim N(0, \sigma = 0.01)$	1.50	1.35	-0.15	-10.00	212	254	42	19.81
	$\sim N(0, \sigma = 0.02)$	1.50	1.27	-0.23	-15.33	212	246	34	16.13
	$\sim N(0, \sigma = 0.03)$	1.50	1.22	-0.28	-18.67	212	188	-24	-11.09

Table 7: Validation results with K-S tests (H_0 : the distance distribution of nominal and estimated defects are sufficiently similar) at 5% significance level for part B with small (local) defects under bending and torsion deformation.

		Bending deformation p-value	Torsion deformation p-value
BUMP #1	Noise-free	0.534	0.318
	$\sim N(0, \sigma = 0.01)$	0.820	0.318
	$\sim N(0, \sigma = 0.02)$	0.891	0.550
	$\sim N(0, \sigma = 0.03)$	0.625	0.318
BUMP #2	Noise-free	0.890	0.433
	$\sim N(0, \sigma = 0.01)$	0.990	0.254
	$\sim N(0, \sigma = 0.02)$	0.998	0.471
	$\sim N(0, \sigma = 0.03)$	0.995	0.791
BUMP #3	Noise-free	0.740	0.997
	$\sim N(0, \sigma = 0.01)$	0.896	0.997
	$\sim N(0, \sigma = 0.02)$	0.999	0.768
	$\sim N(0, \sigma = 0.03)$	0.988	0.997
BUMP #4	Noise-free	0.864	0.957
	$\sim N(0, \sigma = 0.01)$	0.955	0.957
	$\sim N(0, \sigma = 0.02)$	0.931	1.000
	$\sim N(0, \sigma = 0.03)$	0.996	0.982

 H_0 is rejected  H_0 cannot be rejected  H_0 is borderline

Two other validation cases are also applied on part B with a big (global) defect. The nominal size of this defect is illustrated, as a distance distribution, in Figure 20-a. It is compared with results provided by our automatic fixtureless CAI method with bending deformation in Figure 20-b for noise-free scan data. Inspection results for noisy scan meshes (with $\sigma = 0.01, 0.02$ and 0.03 mm) are also shown respectively in Figure 20-c, d, and e. Maximum amplitude and area of estimated defects along with the relative error with respect to the nominal size of defects are summarized in Table 8. Like in the two first cases for part B, these results also show that noise does not generally have a negative effect on the estimation of area and the maximum amplitude of the defect, except for $\sigma = 0.01$ mm. Also, except for $\sigma = 0.01$ mm in this case, amplitude and area of the defect are estimated with good accuracy. As for bending deformation, validation of these results, based on K-S test at a 5% significance level, is

presented in Table 10. These V&V results confirm that the big (global) defect under bending free-state deformation is well estimated, except for $\sigma = 0.01$ mm. This last result (for $\sigma = 0.01$ mm) is due to the presence of high magnitude noise around the defect, which makes that the inspection method filters out too many sample points around the defect. Therefore, the deformed CAD model after FENR cannot correctly compensate for flexible deformation of the scan model. This brings about an inaccurate distance distribution of the defect which leads to overestimating the size of this defect.

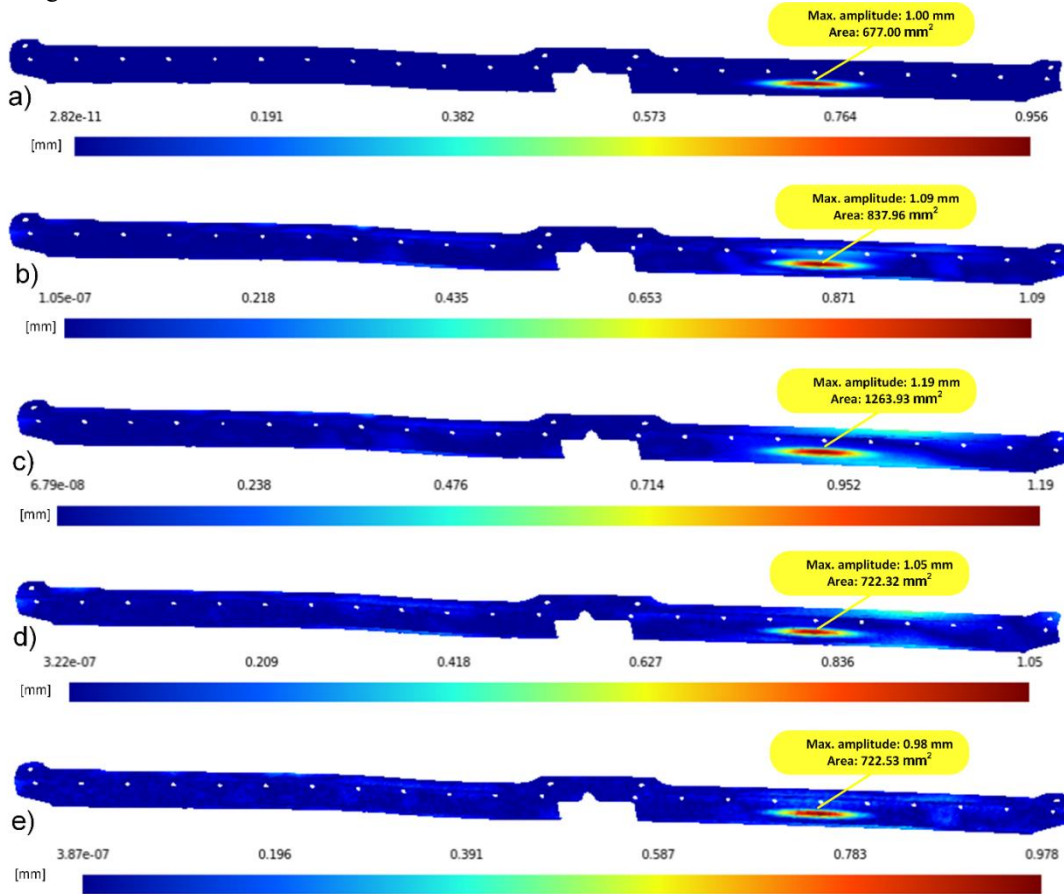


Figure 20: a) nominal defect distance distribution for part B with a big (global) defect, comparison between the CAD and scan model with a big (global) defect and bending deformation as a distance distribution for b) noise-free scan mesh c) noisy scan mesh with $\sigma=0.01$ mm d) noisy scan mesh with $\sigma=0.02$ mm e) noisy scan mesh with $\sigma=0.03$ mm.

Table 8: Estimated size of defects and errors for part B with a big (global) defect and bending deformation.

		Maximum amplitude of defects (D_i^{max})				Area of defects (A_i)			
		Nominal [mm]	Estimated [mm]	Absolute error [mm]	Error [%]	Nominal [mm²]	Estimated [mm²]	Absolute error [mm]	Error [%]
BUMP #1	Noise-free	1.00	1.09	0.09	9.00	677	838	161	23.78
	$\sim N(0, \sigma = 0.01)$	1.00	1.19	0.19	19.00	677	1264	587	86.70
	$\sim N(0, \sigma = 0.02)$	1.00	1.05	0.05	5.00	677	722	45	6.69
	$\sim N(0, \sigma = 0.03)$	1.00	0.98	-0.02	-2.00	677	723	46	6.73

Like in the previous case of part B, the nominal result as distance distribution is compared with estimated results obtained for noise-free along with noisy cases of torsion deformation (see Figure 21). A summary of the inspection results for maximum amplitude and area of estimated defects are presented in Table 9. Here again, these results show that noise does not have a negative effect on the estimation of area and the maximum amplitude of the defect and that amplitude and area of the defect are estimated with good accuracy. Validation of the estimated results based on K-S test at 5% significance level is also presented in Table 10. In this case, V&V results are satisfying.

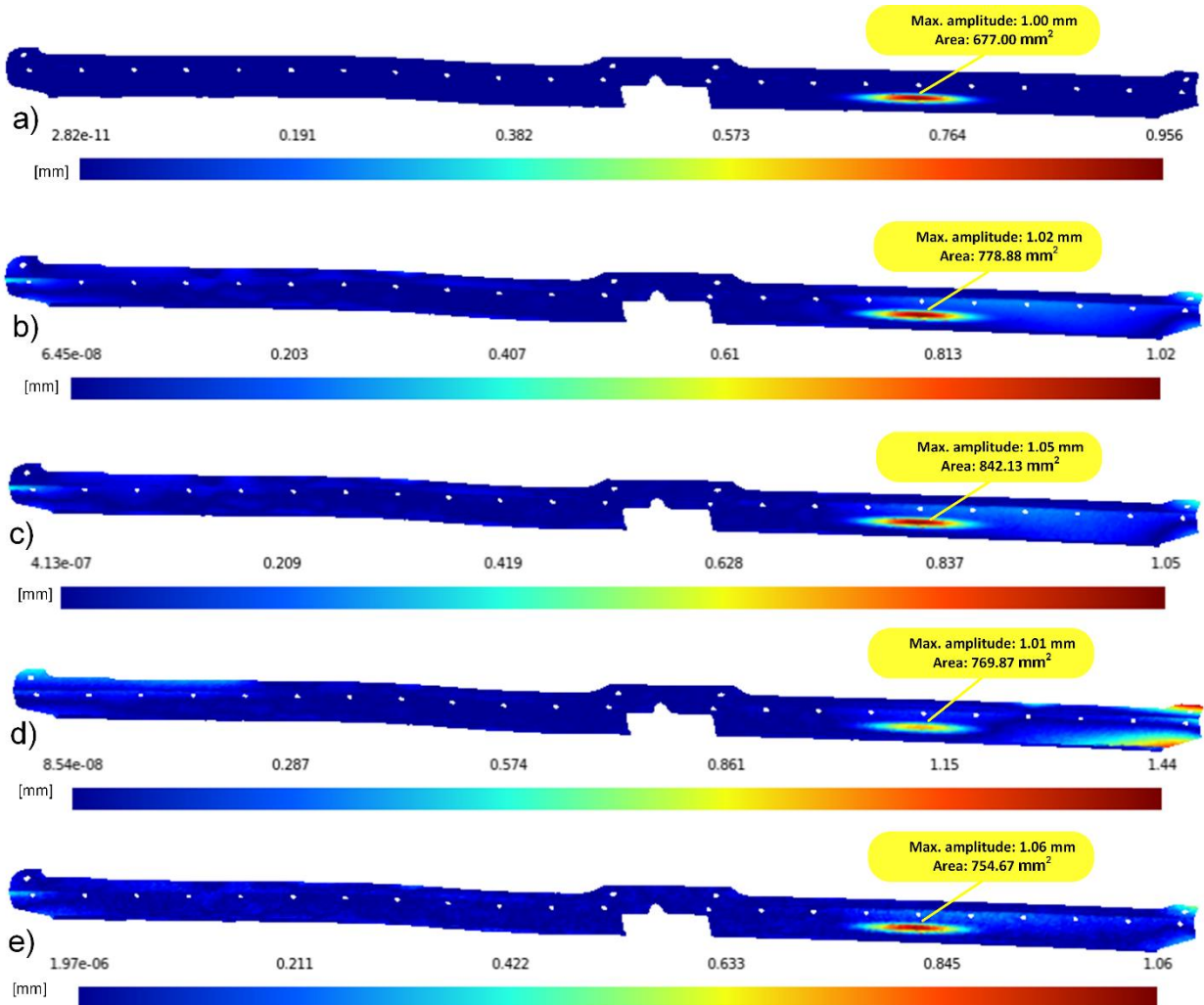


Figure 21: a) nominal defect distance distribution for part B with a big (global) defect, comparison between the CAD and scan model with a big (global) defect and torsion deformation as a distance distribution for b) noise-free scan mesh c) noisy scan mesh with $\sigma=0.01$ mm d) noisy scan mesh with $\sigma=0.02$ mm e) noisy scan mesh with $\sigma=0.03$ mm.

Table 9: Estimated size of defects and errors for part B with a big (global) defect and torsion deformation.

		Maximum amplitude of defects (D_i^{max})				Area of defects (A_i)			
		Nominal [mm]	Estimated [mm]	Absolute error [mm]	Error [%]	Nominal [mm ²]	Estimated [mm ²]	Absolute error [mm ²]	Error [%]
BUMP #1	Noise-free	1.00	1.02	0.02	2.00	677	779	102	15.05
	$\sim N(0, \sigma = 0.01)$	1.00	1.05	0.05	5.00	677	842	165	24.39
	$\sim N(0, \sigma = 0.02)$	1.00	1.01	0.01	1.00	677	770	93	13.72
	$\sim N(0, \sigma = 0.03)$	1.00	1.06	0.06	6.00	677	755	78	11.47

Table 10: Validation results with K-S tests (H_0 : the distance distribution of nominal and estimated defects are sufficiently similar) at 5% significance level for part B with a big (global) defect and under bending and torsion deformation.

BUMP #1		Bending deformation	Torsion deformation
		p-value	p-value
BUMP #1	Noise-free	0.115	0.687
	$\sim N(0, \sigma = 0.01)$	0.015	0.475
	$\sim N(0, \sigma = 0.02)$	0.853	0.525
	$\sim N(0, \sigma = 0.03)$	0.937	0.549

H_0 is rejected
 H_0 cannot be rejected
 H_0 is borderline

4.4. Conclusions about validation cases for part B

Figure 22 summarizes, for part B, the variation of error, on the maximum amplitude and on the area of estimated defects, with respect to noise amplitude. It shows intervals in which errors are distributed for each level of noise from noise-free cases to the noisiest cases ($\sigma = 0.01, 0.02$ and 0.03 mm). This figure illustrates that, in this case, error intervals do not extend when noise amplitude increases for both amplitude and area of defects. Meanwhile, a slight decrease in the mean absolute error is observed for maximum amplitude and area when noise amplitude increases. This confirms that for part B, the accuracy of results provided by our automatic fixtureless CAI method for non-rigid parts is not affected by the presence of noisy scan data since estimation errors for noisy cases remain in the same order of magnitude as for noise-free cases. No clear trend of results worsening with noise can be observed and it also appears that, in some cases, results are surprisingly improved with the introduction of noise in scanned data.

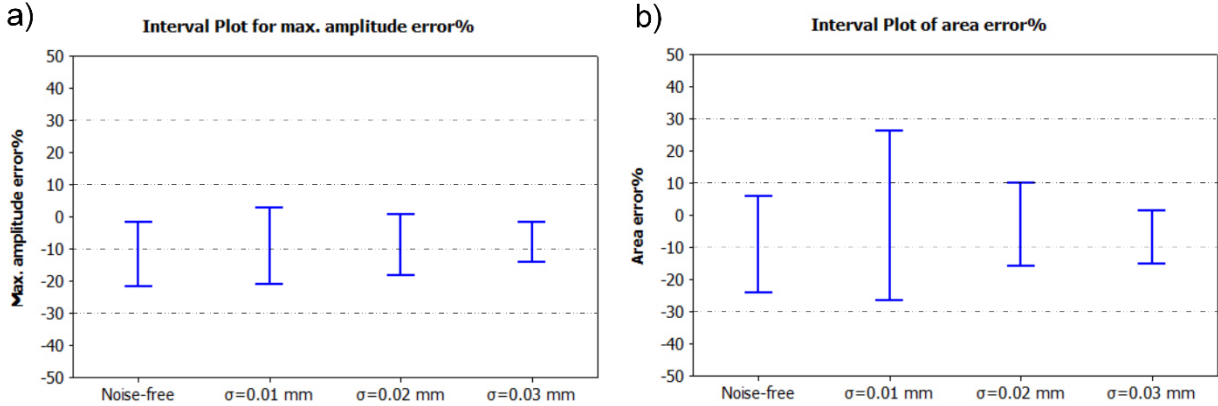


Figure 22: Error intervals for part B with respect to the increase of noise amplitude.

In the results obtained for part B, it seems that maximum amplitude is generally better estimated for big (global) defects than for small (local) defects, but area of defects for this part is slightly better identified for small (local) defects than for big (global) defects. Also, the nature of flexible deformation (bending or torsion) doesn't seem to have an effect on this estimation. As mentioned just above, noise generally does not have a significant effect on the accuracy of results obtained. In some cases, noise improves the accuracy of the estimation. It also shows that some of the identification results are better with torsion deformation than in the case of bending deformation but a clear trend cannot be stated. These results also show that, in the case of small (local) defects, the location of defects has an influence on estimation results, which is not surprising. Indeed, defects are not equally affected by deformation of the part in free-state. This also suggests that, in general, results for a given defect are likely to be affected by the type of free-state deformation.

It has been found in several cases that noise surprisingly tends to improve estimation results. This can be explained considering the fact that the introduction of randomly distributed noise applied to the scan mesh does not necessarily tend to filter more sample points. It appears that, in some cases, noise tends to decrease the final number of sample points used but it also appears that, in other cases, it tends to increase the final number of sample points used. This explains why the introduction of noise can either improve or worsen the estimation of defects. Indeed, for a given case, there is globally an optimal density of sample points for obtaining the most accurate estimation results. Using too many sample points makes that sample points that are too close to defects are used, which worsens estimation results. Not using enough sample points makes that the free-state deformation is not captured accurately enough, which also worsens estimation results. Therefore, the presence of noise close to a defect will sometimes result in an improvement of inspection results since it will remove more sample points and makes it closer to the optimal density but it will also result, in other cases, in worsening results since the density of sample points will become too low for capturing free-state deformation itself.

5. Effect of large free-state deformation

5.1. Cases considered and results obtained

In this section, we assess the effect of the amplitude of free-state deformation on results obtained. Indeed, in the previous sections, for both part A and part B, free-state deformation (bending and torsion for part B) was consistent with a small displacement assumption. Indeed for both parts and all deformation states maximum displacements

were around 10 mm for approximately 1000 mm long parts. In the two cases presented below part A is used and bending free-state deformation is still applied, but in contrast to Figure 23-a, free-state deformation (shown in Figure 23-b) is not any more consistent with a small displacement assumption. Indeed, maximum bending displacement is now around 75 mm if compared to 10 mm in Figure 23-a. Like in section 4.2, two scan models are considered here: one with 3 small (local) defects and another one with one big (global) defect. It is very important to point out that like in previous sections, these scan models with large flexible deformation are still simulated using a linear FEA formulation, which means using a small displacement FEA formulation.

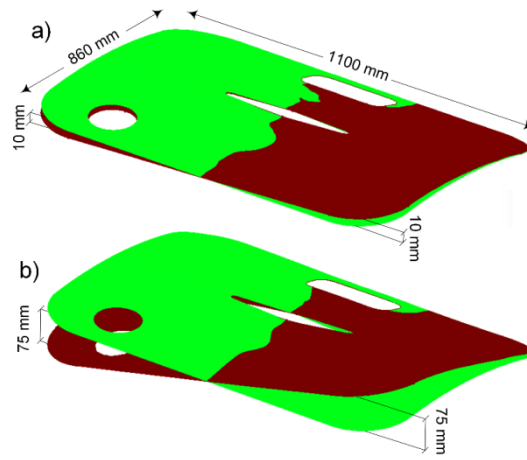


Figure 23: 3D views of CAD model (in green) compared with scan data in a free-state (in brown) for part A with a) small bending deformation b) large bending deformation.

The scan model for the first validation case of part A with large bending deformation includes three small (local) defects. The nominal size of defects (Figure 24-a) is compared with results provided by our automatic fixtureless CAI method in Figure 24-b for noise-free scan data. Inspection results for noisy scan meshes (with $\sigma = 0.01, 0.02$ and 0.03 mm) are also shown respectively in Figure 24-c, d, and e. These estimated distance distributions show that defect areas cannot be correctly detected which leads to a very poor estimation of defects on scan meshes when flexible deformation is large. This large flexible deformation of the scan model in a free-state makes that the CAD model does not correctly match this deformation via FENR. This can be explained considering that FEA, in our method, is based on a linear formulation (small displacement formulation). Using a linear FEA formulation for the registration of models that are subjected to large displacements results in a non-realistic stretching.

Maximum amplitude and area of estimated defects are compared with nominal size of defects in Table 11. Results in Table 11 show that defects are poorly estimated in general, both for maximum amplitude and area.

Like for small free-state deformation in section 4.2, V&V results, based on K-S test at a 5% significance level are presented in Table 12. These results show that distance distributions associated with estimated defects are not similar to the corresponding distance distributions for nominal defects. Indeed, H_0 hypothesis can be rejected in all cases.

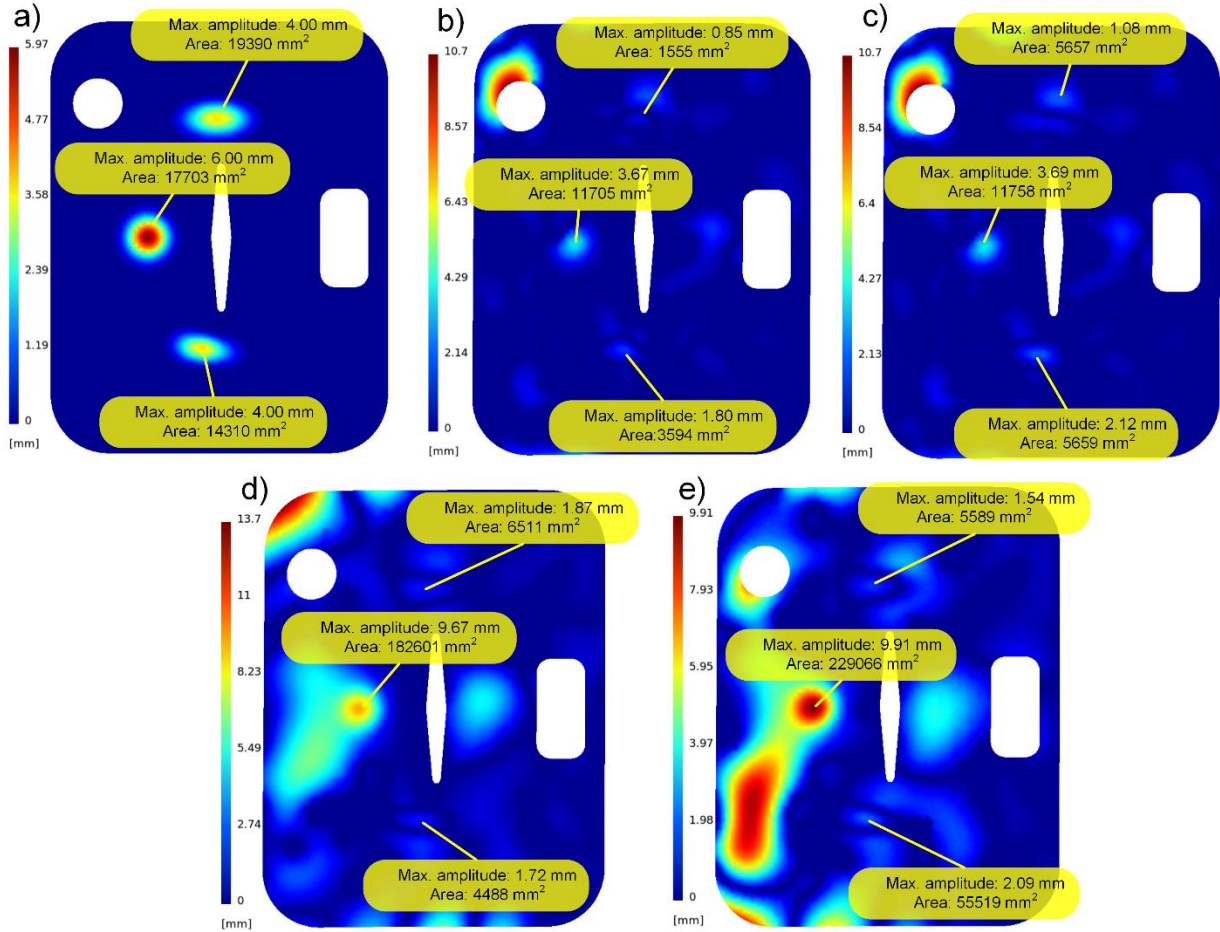


Figure 24: a) nominal defect distance distribution for part A with small (local) defects, comparison between the CAD and scan model of part A with small (local) defects and large bending deformation as a distance distribution for b) noise-free scan mesh c) noisy scan mesh with $\sigma=0.01$ mm d) noisy scan mesh with $\sigma=0.02$ mm e) noisy scan mesh with $\sigma=0.03$ mm.

Table 11: Estimated size of defects and errors for part A with local defects and large bending deformation.

		Maximum amplitude of defects (D_i^{max})				Area of defects (A_i)			
		Nominal [mm]	Estimated [mm]	Absolute error [mm]	Error [%]	Nominal [mm ²]	Estimate d [mm ²]	Absolute error [mm ²]	Error [%]
BUMP #1	Noise-free	4.00	0.85	-3.15	-78.74	19390	1555	-17835	-91.98
	$\sim N(0, \sigma = 0.01)$	4.00	1.08	-2.92	-72.91	19390	5657	-13733	-70.82
	$\sim N(0, \sigma = 0.02)$	4.00	1.87	-2.13	-53.25	19390	6511	-12879	-66.42
	$\sim N(0, \sigma = 0.03)$	4.00	1.54	-2.46	-61.51	19390	5589	-13801	-71.17
BUMP #2	Noise-free	6.00	3.67	-2.33	-38.80	17703	11705	-5998	-33.88
	$\sim N(0, \sigma = 0.01)$	6.00	3.69	-2.31	-38.52	17703	11758	-5945	-33.58
	$\sim N(0, \sigma = 0.02)$	6.00	9.67	3.67	61.20	17703	182601	164898	931.46
	$\sim N(0, \sigma = 0.03)$	6.00	9.91	3.91	65.24	17703	229066	211363	1193.93
BUMP #3	Noise-free	4.00	1.80	-2.20	-54.90	14310	3594	-10717	-74.89
	$\sim N(0, \sigma = 0.01)$	4.00	2.12	-1.88	-47.02	14310	5659	-8652	-60.46
	$\sim N(0, \sigma = 0.02)$	4.00	1.72	-2.28	-57.06	14310	4488	-9822	-68.64
	$\sim N(0, \sigma = 0.03)$	4.00	2.09	-1.91	-47.72	14310	55519	41209	287.97

Table 12: Validation results with K-S tests (H_0 : the distance distribution of nominal and estimated defects are sufficiently similar) at 5% significance level for part A with local defects and large bending deformation.

		p-value
BUMP #1	Noise-free	0.000
	$\sim N(0, \sigma = 0.01)$	0.000
	$\sim N(0, \sigma = 0.02)$	0.000
	$\sim N(0, \sigma = 0.03)$	0.000
BUMP #2	Noise-free	0.000
	$\sim N(0, \sigma = 0.01)$	0.000
	$\sim N(0, \sigma = 0.02)$	0.004
	$\sim N(0, \sigma = 0.03)$	0.000
BUMP #3	Noise-free	0.000
	$\sim N(0, \sigma = 0.01)$	0.002
	$\sim N(0, \sigma = 0.02)$	0.000
	$\sim N(0, \sigma = 0.03)$	0.000

H_0 is rejected
 H_0 cannot be rejected
 H_0 is borderline

In the next case, a big (global) defect is considered on part A with a large bending deformation. Nominal and estimated sizes of defects are compared (see Figure 25) and V&V results are provided. Like in the previous case, results presented in Table 13 show that defects are poorly estimated both for maximum amplitude and area. Using K-S test at 5% significance level for validating the inspection results for this case, with noise-free and noisy scan meshes (with $\sigma = 0.01, 0.02$ and 0.03 mm) results in “ H_0 is rejected” in all cases. As just explained above, the CAD model via linear FENR cannot correctly follow the shape of scan model with a large flexible deformation. The CAD model is stretched during FENR which leads to incorrect distance distributions and consequently incorrect estimations of the size of defects.

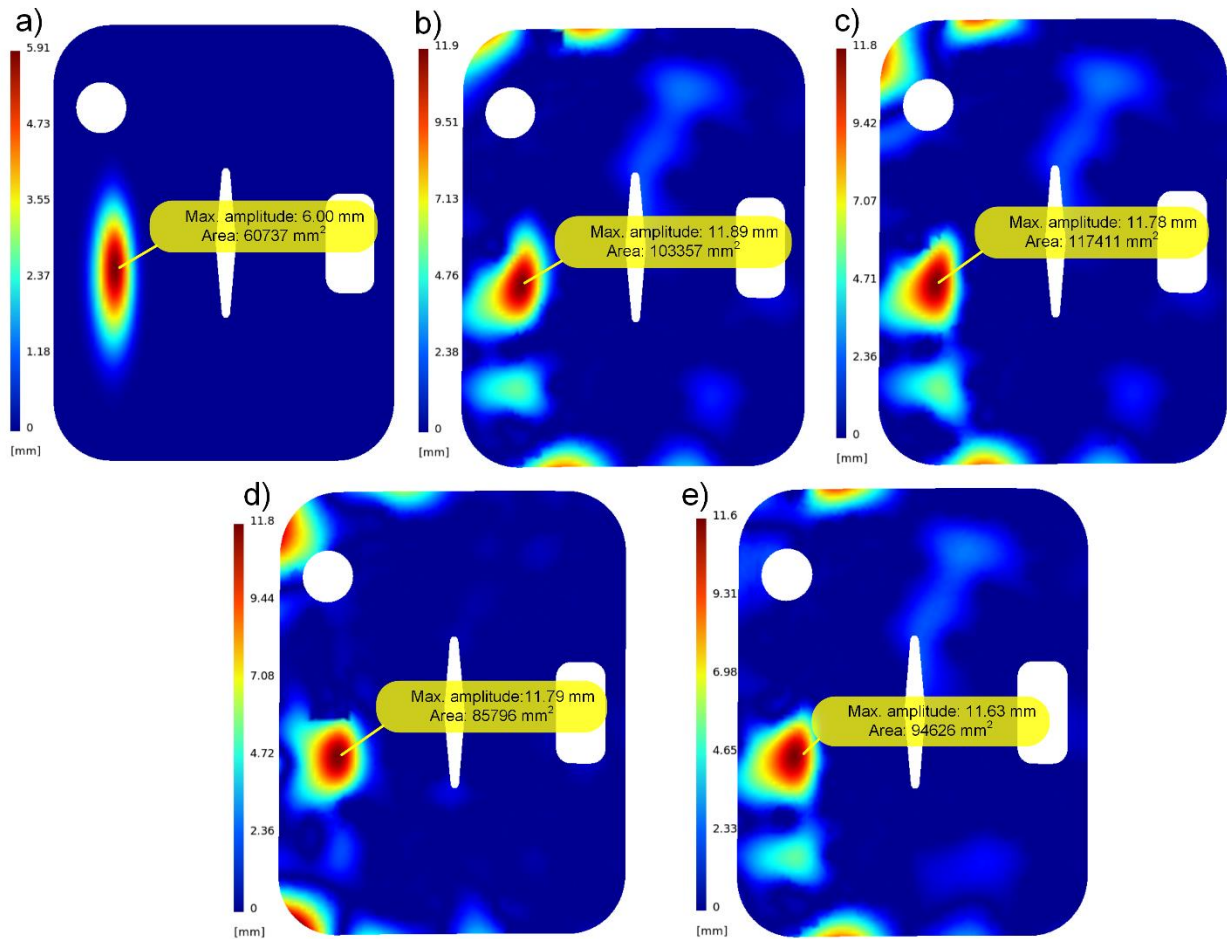


Figure 25: a) nominal defect distance distribution for part A with a global defect, comparison between the CAD and scan model of part A with a global defect and large bending deformation as a distance distribution for b) noise-free scan mesh c) noisy scan mesh with $\sigma=0.01$ mm d) noisy scan mesh with $\sigma=0.02$ mm e) noisy scan mesh with $\sigma=0.03$ mm.

Table 13: Estimated size of defects and errors for part A with a global defect and large bending deformation.

		Maximum amplitude of defects (D_i^{max})				Area of defects (A_i)			
		Nominal [mm]	Estimated [mm]	Absolute error [mm]	Error [%]	Nominal [mm ²]	Estimated [mm ²]	Absolute error [mm]	Error [%]
BUMP #1	Noise-free	6.00	11.89	5.89	98.15	60737	103357	42620	70.17
	$\sim N(0, \sigma = 0.01)$	6.00	11.78	5.78	96.28	60737	117411	56674	93.31
	$\sim N(0, \sigma = 0.02)$	6.00	11.79	5.79	96.57	60737	85796	25059	41.26
	$\sim N(0, \sigma = 0.03)$	6.00	11.63	5.63	93.87	60737	94626	33889	55.80

5.2. Conclusions about the effect of large free-state deformation

Results presented in the previous section clearly show that the amplitude of free-state deformation has a major effect on inspection results. Indeed, for the two cases featuring a large free-state deformation, inspection results are a lot worse than inspection results obtained for corresponding cases featuring small deformation, as presented in section 4.2. The same trend is observed for both the assessment of maximum amplitude and area of defects and V&V results, which is not surprising. Indeed, if the maximum amplitude and area of defects are badly estimated, distance distributions associated with nominal and estimated defects are not expected to be very similar.

Figure 26 presents a comparison between results obtained for small and large free-state deformation on part A. Figure 26-a summarizes cases with three small (local) defects (as presented in Table 1 and maximum amplitude and area of estimated defects are compared with the nominal size of defects in Table 11. Results in Table 11 show that defects are poorly estimated in general, both for maximum amplitude and area. Like for small free-state deformation

in section 4.2, V&V results, based on K-S test at a 5% significance level are presented in Table 12. These results show that distance distributions associated with estimated defects are not similar to the corresponding distance distributions for nominal defects. Indeed, H_0 hypothesis can be rejected in all cases.

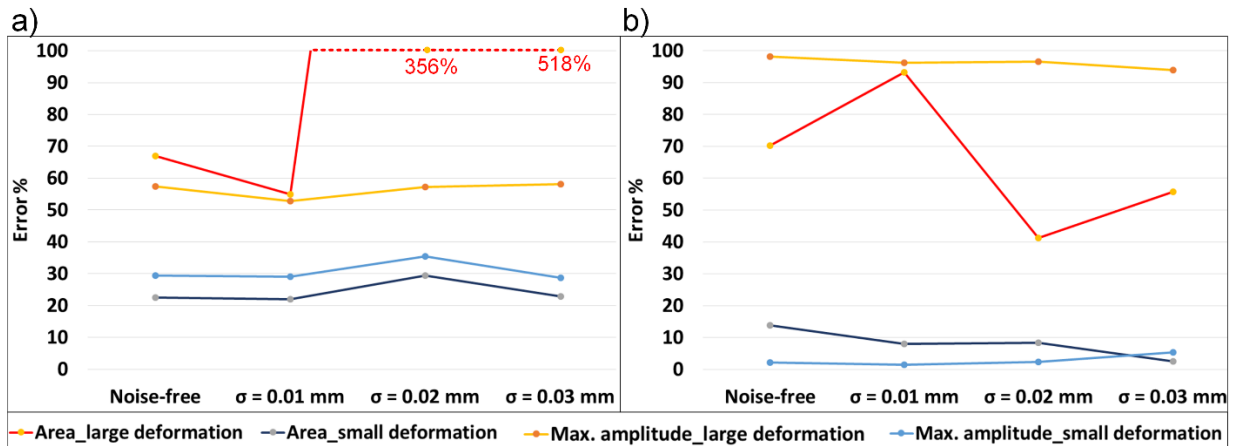


Figure 26: Absolute error (in %) in the estimation of defects for part A for small versus large deformation.

Figure 26 clearly shows the degradation of results brought about by large free-state deformation for the two considered cases and for both estimations of maximum amplitude and area of defects. This degradation is not surprising since, in all cases, a linear FEA formulation has been used for both simulating scanned data and finite element non-rigid registration (FENR). Indeed linear FEA formulations are based on a small displacement assumption and as much as free-state deformation increases, this assumption is less and less verified, which explains the trend shown about the degradation of inspection results. Going further in the comparison between inspection results obtained with small and large free-state deformation, it appears in Table 1, and maximum amplitude and area of estimated defects are compared with the nominal size of defects in Table 11. Results in Table 11 show that defects are poorly estimated in general, both for maximum amplitude and area.

Like for small free-state deformation in section 4.2, V&V results, based on K-S test at a 5% significance level are presented in Table 12. These results show that distance distributions associated with estimated defects are not similar to the corresponding distance distributions for nominal defects. Indeed, H_0 hypothesis can be rejected in all cases.

Table 11 shows that the degradation of results for Bump #2 is globally more severe than for Bump #1 and Bump #3. Looking at Figure 6-a and Figure 23, it appears that Bump #2 is located in a zone that is likely to be more affected than others by the free-state deformation. This may explain why the degradation is more severe for Bump #2 than for Bump #1 and Bump #3. This is confirmed when comparing results shown in Table 3 and Table 13 for the case with a big (global) defect only. In this case, the degradation of inspection results with large free-state deformation is even more severe as globally illustrated in Figure 26-b. Indeed this big (global) defect is located in the same zone than Bump #2 in the case with three small (local) defects.

As introduced above, this degradation of inspection results with large free-state deformation can be explained considering that both the simulation of free-state deformation and FENR are performed using a linear FEA formulation, thus based on a small displacement hypothesis. Applying a linear FEA formulation to problems featuring large displacement results in unwanted and non-realistic stretching that is likely to affect the shape of defects and by the way inspection results. Of course, this non-realistic stretching increases with free-state deformation which increases the degradation of inspection results. It is worth noting that this non-realistic stretching adds to the effect of GNIF accuracy, which also causes non-realistic stretching and also directly and negatively affects inspection results. Moreover, it tends to decrease GNIF accuracy itself since GNIF is based on the assumption that the deformation of a non-rigid part in free-state is isometric (preserves geodesic distances). Indeed, in the context of large displacement in free-state, this isometry assumption requires using a large displacement FEA formulation to be fulfilled. As mentioned in the conclusion, this is part of our plans for future work on the subject.

6. Conclusion

This paper proposes a metric aimed at validating an automatic fixtureless Computer-Aided Inspection (CAI) method for non-rigid parts. This CAI method is based on establishing a correspondence between scan and CAD data through sets of sample points, on filtering sample points that may be close to defects and on finite element non-rigid registration (FENR). This metric allows assessing the similarity of distance distribution for the estimated defects, which are identified with our inspection method, in comparison with that of nominal defects on a manufactured part. The metric applies statistical hypothesis testing, namely the Kolmogorov–Smirnov (K-S) test, to make comparisons

between cumulative distribution functions (CDFs) associated with estimated and nominal defects. Robustness of the CAI method is validated by adding noise to the scan data. Applying this validation process to CAI results obtained on two aerospace parts shows that the assessment of maximum amplitude and area of estimated defects is not significantly affected by noise since error distributions remain in the same magnitude of magnitude. Results obtained from K-S tests with respect to the ability of the CAI method in assessing distance distributions of estimated defects also infer that, in general, the method provides sufficiently accurate results and that distance distributions of estimated defects can be reasonably well identified. These results show that the accuracy of a CAI depends on the magnitude of flexible deformation applied on the scan model, especially in the vicinity of defects, but the nature of flexible deformation (bending or torsion) as well as the nature of defects (small (local) or big (global) defects) does not have a significant effect on the inspection accuracy.

It is important to underline that the validation metric proposed in this paper is not restricted to assessing the performance of our CAI method. Applying it to our method is an example of what can be done in many other contexts. For metrology purposes, this metric can indeed be successfully applied to any CAI method, since the only input data required is sets of distance distributions between CAD geometry and scanned geometry. Thus, a natural extension of this work would be applying this validation metric to other CAI approaches.

Even if these validation results are promising, they reveal that several improvements can be foreseen towards improving this CAI method with respect to its different sources of uncertainty. Improving accuracy of the non-rigid registration method used (GNIF) would be a first interesting step forward. We found out that the main source of inaccuracy in applying GNIF is related to sources of inaccuracy in fast marching calculations underlying GNIF. We are presently investigating numerical strategies that should improve the accuracy of fast marching results. Also, since the inspection method is based on discretized curvature calculation and FEA, the mesh size and its quality especially on features with high curvatures can be a source of error on the estimation of defects in the final inspecting results. Meanwhile, all free-state flexible deformations in scan models are considered as linear, which means in the small displacement hypothesis range and that FENR is performed using linear FEA calculations. As shown in section 5, this hypothesis is not verified in many practical cases. Consequently, a natural extension of this work is setting up an extension of this CAI method based on a large displacement FEA formulation. Results obtained using a large displacement FEA formulation could be compared with results obtained using the point drift (CPD) algorithm [48]. This algorithm is indeed a promising non-FEA-based inspection method that shows, in some cases, good efficiency for large flexible deformation.

7. Acknowledgment

The authors would like to thank the National Sciences and Engineering Research Council of Canada (NSERC), industrial partners, Consortium for Aerospace Research and Innovation in Québec (CRIAQ) and UQTR foundation for their support and financial contribution. In this paper, we use GmshTM [47] for visualizing meshes, stress, curvature and error distributions.

8. References

- [1] G. N. Abenham, A. Desrochers, and A. Tahan, "Nonrigid parts' specification and inspection methods: notions, challenges, and recent advancements," *International Journal of Advanced Manufacturing Technology*, vol. 63, pp. 741-752, Nov 2012.
- [2] G. N. Abenham, S. A. Tahan, A. Desrochers, and J.-F. Lalonde, "Aerospace Panels Fixtureless Inspection Methods with Restraining Force Requirements; A Technology Review," SAE Technical Paper 2013.
- [3] A. Weckenmann and J. Weickmann, "Optical Inspection of Formed Sheet Metal Parts Applying Fringe Projection Systems and Virtual Fixation," *Metrology and Measurement Systems*, vol. 13, pp. 321-330, 2006.
- [4] I. Gentilini and K. Shimada, "Predicting and evaluating the post-assembly shape of thin-walled components via 3D laser digitization and FEA simulation of the assembly process," *Computer-aided design*, vol. 43, pp. 316-328, 2011.
- [5] G. N. Abenham, A. Desrochers, A. S. Tahan, and J. Bignon, "A virtual fixture using a FE-based transformation model embedded into a constrained optimization for the dimensional inspection of nonrigid parts," *CAD Computer Aided Design*, vol. 62, pp. 248-258, 2015.
- [6] A. Weckenmann, J. Weickmann, and N. Petrovic, "Shortening of inspection processes by virtual reverse deformation," in *4th international conference and exhibition on design and production of machines and dies/molds, Cesme, Turkey, 2007*.
- [7] A. Jaramillo, F. Prieto, and P. Boulanger, "Fixtureless inspection of deformable parts using partial captures," *International Journal of Precision Engineering and Manufacturing*, vol. 14, pp. 77-83, 2013.
- [8] G. N. Abenham, A. S. Tahan, A. Desrochers, and R. Maranzana, "A Novel Approach for the Inspection of Flexible Parts Without the Use of Special Fixtures," *Journal of Manufacturing Science and Engineering-Transactions of the Asme*, vol. 133, Feb 2011.

- [9] A. Aidibe, A. S. Tahan, and G. N. Abenham, "Distinguishing profile deviations from a part's deformation using the maximum normed residual test," *WSEAS Transactions on Applied & Theoretical Mechanics*, vol. 7, 2012.
- [10] H. Radvar-Esfahlan and S.-A. Tahan, "Nonrigid geometric metrology using generalized numerical inspection fixtures," *Precision Engineering*, vol. 36, pp. 1-9, 2012.
- [11] V. Sabri, S. A. Tahan, X. T. Pham, D. Moreau, and S. Galibois, "Fixtureless profile inspection of non-rigid parts using the numerical inspection fixture with improved definition of displacement boundary conditions," *International Journal of Advanced Manufacturing Technology*, vol. 82, pp. 1343-1352, 2016.
- [12] S. Sattarpanah Karganroudi, J.-C. Cuillière, V. Francois, and S.-A. Tahan, "Automatic fixtureless inspection of non-rigid parts based on filtering registration points," *The International Journal of Advanced Manufacturing Technology*, pp. 1-26, 2016.
- [13] A. Weckenmann, P. Gall, and J. Hoffmann, "Inspection of holes in sheet metal using optical measuring systems," in *Proceedings of VIth International Science Conference Coordinate Measuring Technique (April 21-24, 2004, Bielsko-Biala, Poland)*, 2004, pp. 339-346.
- [14] L. Schwer, H. Mair, and R. Crane, "Guide for verification and validation in computational solid mechanics," *American Society of Mechanical Engineers, ASME V&V*, vol. 10.1, 2012.
- [15] P. J. Besl and N. D. McKay, "A Method for Registration of 3-D Shapes," *Ieee Transactions on Pattern Analysis and Machine Intelligence*, vol. 14, pp. 239-256, Feb 1992.
- [16] A. M. Bronstein, M. M. Bronstein, and R. Kimmel, "Generalized multidimensional scaling: A framework for isometry-invariant partial matching," *Proceedings of the National Academy of Sciences of the United States of America*, vol. 103, pp. 1168-1172, 2006.
- [17] R. Kimmel and J. A. Sethian, "Computing geodesic paths on manifolds," *Proceedings of the National Academy of Sciences*, vol. 95, pp. 8431-8435, 1998.
- [18] H. Borouchaki, P. L. George, and S. H. Lo, "Optimal delaunay point insertion," *International Journal for Numerical Methods in Engineering*, vol. 39, pp. 3407-3437, 1996.
- [19] A. AIAG, "Measurement systems analysis (MSA)," *Reference Manual, Fourth Edition, The Automotive Industries Action Group, Troy*, 2010.
- [20] W. L. Oberkampf, T. G. Trucano, and C. Hirsch, "Verification, validation, and predictive capability in computational engineering and physics," *Applied Mechanics Reviews*, vol. 57, pp. 345-384, 2004.
- [21] D. Sornette, A. Davis, K. Ide, K. Vixie, V. Pisarenko, and J. Kamm, "Algorithm for model validation: Theory and applications," *Proceedings of the National Academy of Sciences*, vol. 104, pp. 6562-6567, 2007.
- [22] W. L. Oberkampf and M. F. Barone, "Measures of agreement between computation and experiment: Validation metrics," *Journal of Computational Physics*, vol. 217, pp. 5-36, 2006.
- [23] R. G. Hills and T. G. Trucano, "Statistical validation of engineering and scientific models: Background," *Sandia National Laboratories, Albuquerque, NM, Report No. SAND99-1256*, 1999.
- [24] A. S. Committee, "AIAA Guide for the Verification and Validation of Computational Fluid Dynamics Simuations (G-077-1998)," ed: AIAA, 1998.
- [25] V. Committee, "Standard for verification and validation in computational fluid dynamics and heat transfer," *American Society of Mechanical Engineers, New York*, 2009.
- [26] B. Cowles, D. Backman, and R. Dutton, "Verification and validation of ICME methods and models for aerospace applications," *Integrating Materials and Manufacturing Innovation*, vol. 1, pp. 1-16, 2012.
- [27] Y. Liu, W. Chen, P. Arendt, and H. Z. Huang, "Toward a better understanding of model validation metrics," *Journal of Mechanical Design, Transactions of the ASME*, vol. 133, 2011.
- [28] W. L. Oberkampf and T. G. Trucano, "Verification and validation benchmarks," *Nuclear engineering and Design*, vol. 238, pp. 716-743, 2008.
- [29] S. Ferson and W. L. Oberkampf, "Validation of imprecise probability models," *International Journal of Reliability and Safety*, vol. 3, pp. 3-22, 2009.
- [30] J. P. Kleijnen, "Statistical validation of simulation models," *European Journal of Operational Research*, vol. 87, pp. 21-34, 1995.
- [31] T. Buranathiti, J. Cao, W. Chen, L. Baghdasaryan, and Z. C. Xia, "Approaches for model validation: methodology and illustration on a sheet metal flanging process," *Journal of Manufacturing Science and Engineering*, vol. 128, pp. 588-597, 2006.
- [32] T. L. Paez and A. Urbina, "Validation of mathematical models of complex structural dynamic systems," in *Proceedings of the ninth international congress on sound and vibration, Orlando, FL*, 2002.
- [33] R. G. Hills and I. H. Leslie, "Statistical validation of engineering and scientific models: validation experiments to application," Sandia National Labs., Albuquerque, NM (US); Sandia National Labs., Livermore, CA (US)2003.

- [34] K. J. Dowding, I. H. Leslie, M. L. Hobbs, B. M. Rutherford, R. G. Hills, and M. M. Pilch, "Case study for model validation: assessing a model for thermal decomposition of polyurethane foam," Sandia National Laboratories 2004.
- [35] B. Rutherford and K. Dowding, "An approach to model validation and model-based prediction—polyurethane foam case study," *SAND2003-2336, Sandia National Laboratories, Albuquerque*, 2003.
- [36] W. Chen, L. Baghdasaryan, T. Buranathiti, and J. Cao, "Model validation via uncertainty propagation and data transformations," *ALAA journal*, vol. 42, pp. 1406-1415, 2004.
- [37] R. Rebba and S. Mahadevan, "Computational methods for model reliability assessment," *Reliability Engineering & System Safety*, vol. 93, pp. 1197-1207, 2008.
- [38] R. B. D'Agostino, *Goodness-of-fit-techniques* vol. 68: CRC press, 1986.
- [39] R. G. Ghanem, A. Doostan, and J. Red-Horse, "A probabilistic construction of model validation," *Computer Methods in Applied Mechanics and Engineering*, vol. 197, pp. 2585-2595, 2008.
- [40] F. J. Massey Jr, "The Kolmogorov-Smirnov test for goodness of fit," *Journal of the American statistical Association*, vol. 46, pp. 68-78, 1951.
- [41] S. Mahadevan and A. Haldar, *Probability, reliability and statistical method in engineering design*: John Wiley & Sons, 2000.
- [42] X. Sun, P. L. Rosin, R. R. Martin, and F. C. Langbein, "Noise in 3D laser range scanner data," in *Shape Modeling and Applications, 2008. SMI 2008. IEEE International Conference on*, 2008, pp. 37-45.
- [43] C. Boehnen and P. Flynn, "Accuracy of 3D scanning technologies in a face scanning scenario," in *3-D Digital Imaging and Modeling, 2005. 3DIM 2005. Fifth International Conference on*, 2005, pp. 310-317.
- [44] J. R. Diebel, S. Thrun, and M. Brünig, "A Bayesian method for probable surface reconstruction and decimation," *ACM Transactions on Graphics (TOG)*, vol. 25, pp. 39-59, 2006.
- [45] M. Alexa, "Wiener filtering of meshes," in *Shape Modeling International, 2002. Proceedings*, 2002, pp. 51-57.
- [46] J. C. Cuillière and V. Francois, "Integration of CAD, FEA and topology optimization through a unified topological model," *Computer-Aided Design and Applications*, vol. 11, pp. 1-15, // 2014.
- [47] C. Geuzaine and J.-F. Remacle, "Gmsh: a three-dimensional finite element mesh generator with built-in pre- and post-processing facilities," *International Journal for Numerical Methods in Engineering*, vol. 79, pp. 1309-1331, 2009.
- [48] A. Aidibe and A. Tahan, "Adapting the coherent point drift algorithm to the fixtureless dimensional inspection of compliant parts," *International Journal of Advanced Manufacturing Technology*, vol. 79, pp. 831-841, 2015.